General Disclaimer

One or more of the Following Statements may affect this Document

- This document has been reproduced from the best copy furnished by the organizational source. It is being released in the interest of making available as much information as possible.

- This document may contain data, which exceeds the sheet parameters. It was furnished in this condition by the organizational source and is the best copy available.

- This document may contain tone-on-tone or color graphs, charts and/or pictures, which have been reproduced in black and white.

- This document is paginated as submitted by the original source.

- Portions of this document are not fully legible due to the historical nature of some of the material. However, it is the best reproduction available from the original submission.

An Analysis of Carbon^{14} Radiation Detection Systems

Task I Final Report
Contract NAS 25546
BSR 2781
October 1969

Ann Arbor, Michigan

Bendix Aerospace Systems Division

An Analysis of Carbon^{14} Radiation Detection Systems

Task I Final Report
Contract NAS 25546
BSR 2781
October 1969

Ann Arbor, Michigan

Submitted to:

National Aeronautics and
Space Administration
Ames Research Center
Moffett Field, California 94035

Prepared by K. Wainio

Approved by W L Rogers

Approved by T. H. Colvin

Bendix Aerospace Systems Division

TABLE OF CONTENTS

TABLE OF CONTENTS (CONT.)

TABLE OF CONTENTS (CONT.)

LIST OF ILLUSTRATIONS

LIST OF TABLES

SECTION 1

INTRODUCTION AND SUMMARY

This Task I report is part of an overall evaluation of C^{14} detection concepts for possible use in life detection experiments to be conducted in unmanned missions to Mars. The current science definition lists three categories of experiments under consideration for these missions which require detection of C^{14} beta particles.

Category A - In this type of experiment, soil which may contain micro-organisms is exposed to C^{14} labelled organic nutrients. Biological activity would cause the evolution of C^{14} labelled carbon dioxide ($C^{14}O_2$).

Category B - This experiment is designed to detect the dark release of $C^{14}O_2$ from soil samples which have been incubated in a labelled carbon dioxide atmosphere under conditions of Martian daylight. It is similar to the CO_2 evolution (Category A) experiment in that the volume of gas involved is small.

Category C - In this type of experiment, soil which may contain micro-organisms is exposed to $C^{14}O_2$. Biological activity would synthesize C^{14} labelled organic compounds from the $C^{14}O_2$. The excess of $C^{14}O_2$ is then removed by an inert carrier gas purge. The soil sample is then pyrolyzed in the carrier gas stream. Pyrolysis products from any C^{14} labelled organic compounds include CO, CO_2, water volatile organic compounds, non-volatile organic compounds and elemental carbon. The non-volatiles remain with the sample. Water, CO, and CO_2 pass through a gas chromatograph column, a copper oxide (CuO) column, and reach the detection system where radioactivity is measured. The volatile organic compounds are retained in the gas chromatograph column. The volatile organic compounds are then eluted from the column by heating and carrier gas purging. These compounds are oxidized to CO_2 and water in the CuO column, and are passed to the detection system for a radioactivity measurement. This second activity measurement is separate and distinct from the first. In both radioactivity measurements, quench gas is added if required.

The objective of the Task I analysis was to analyze the various types of C^{14} detection techniques and determine the most effective techniques which will then be breadboarded and evaluated in Task II of this study. The emphasis was placed on calculating relative performance of the different detectors. The absolute efficiencies and count rates listed will, of course, be considerably less accurate. It should be further realized that the state of the art may change drastically over the next year or two so that this report cannot draw any final conclusions regarding detector choices for the Life Detection Experiment.

1.1 C^{14} DETECTION TECHNIQUES

The two principal detection techniques investigated in the study are described below.

1.1.1 Pairs of Detectors in 4π- Geometry

In this detector concept, a pair of small detectors are mounted face-to-face and the C^{14} gas is introduced into the sensitive volume between the detectors. This type of detection system is being considered for the Category A and B experiments in which the volume of gas evolved will be relatively small. The separation between the detectors can therefore be on the order of the detector radius or less so the geometric efficiency of the pair of detectors will be high, although not truly equal to 4π unless the separation is zero. The paired detector concept also makes it possible to employ coincidence techniques to reduce background count rates.

The types of detectors considered for use in this concept includes pairs of: (1) thin window pancake detectors, (2) surface barrier detectors, (3) avalanche detectors, (4) diffused junction detectors, and (5) lithium drifted detectors. Analyses were performed to determine the optimum detector type and detector geometry for use in the Category A and B experiments.

1.1.2 Plastic Scintillation Detector

In the Category C experiment, the C^{14} will be carried in the effluent gases from a gas chromatograph so the sensitive detector volumes must be larger than is required with the Category A experiments. The detector considered for these experiments is a thin wall plastic scintillator enclosing a C^{14} gas volume of about 20 cc. The thin plastic scintillator will be wrapped in a CsI(Na) scintillator or second plastic scintillator to permit coincidence

rejection of background radiations. This is a new detector concept which will be tested extensively during the Task II breadboard phase of this contract. Preliminary experiments conducted thus far have been very encouraging both in regard to C^{14} beta detection efficiency in the plastic scintillator and to coincidence rejection of Cs^{137} and Co^{60} gamma ray background radiation.

1.1.3 Other Detection Techniques

A logical candidate for the Category C detector is an internal gas proportional counter; however, the internal gas proportional counter has been specifically excluded from consideration in this study.

Some consideration has been given to developing a multianode geiger tube. The C^{14} gas would be introduced into the central volume of the detector and retained by a thin membrane. This membrane would then be surrounded by two concentric multianode geiger counters. The outer counter would serve as a guard counter and the inner counter as the beta detector. The two counters would be separated by a wall just thick enough to prevent the C^{14} betas from entering the guard counter.

The rationale behind this design is to provide a beta counter and guard counter which are separated by a minimum amount of material so as to minimize the sensitivity of the detector to gamma rays. In addition the aim is to have good geometry gas counting without having to worry about contaminants in the counting gas. However, the detector concept also has several inherent disadvantages. First, it would probably be difficult to develope a thin, but strong membrane that will be capable of supporting the C^{14} gas in the center of the counter for all the fill gas pressures and volumes that might be encountered in the life detection experiments. Any distortion of the C^{14} volume would alter the gas pressure in the surrounding counter and alter its sensitivity. Also, problems would undoubtedly be encountered in designing the anode structures so as to provide reliable and uniform (4π) detection sensitivity. The problems associated with the development of the plastic scintillation detector are not expected to be as difficult as those associated with the multianode geiger detector and, of greater importance, the plastic scintillator is expected to have greater C^{14} detection capability. Therefore, the multianode geiger tube concept has been discarded, and the plastic scintillator will be evaluated in the Task II breadboard phase.

The paired detector concept could be improved by utilizing four detectors arranged so that the detector faces lie on the surfaces of a tetrahedron. Both C^{14} detection efficiency and background rejection should be improved with this geometry, and, by enlarging the C^{14} gas volume, it could be employed in Category A, B, and C experiments. The use of four detectors would also be advantageous from the standpoint of system reliability since the failure of a single detector would not preclude successful completion of the experiment. This detector design will not be evaluated in the Task II breadboards since it is only a geometric modification of the paired detector system. The needed information on detector performance can more readily be obtained with the paired detector geometry.

The use of getters has not been considered in the evaluation of the paired detector concept. With a getter, the detector separation can be made essentially zero and the pair will have 4π detection efficiency. Furthermore smaller diameter, lower noise detectors could be used without sacrificing geometric efficiency. Gettering won't have a strong effect on the relative evaluation of detector types but will affect the absolute sensitivity and experimental complexity. Some measurements are being made of the effectiveness of gettering as part of the Life Detection Experiments and the results will be available at the completion of the contract.

1.2 CONCLUSIONS

Table 1-1 summarizes the results obtained for the various detectors considered in this study. The Task I analysis has shown that the semiconductor detectors generally will perform more satisfactorily than thin window pancake detectors in the paired detector geometry for Category A experiments. The detector performance is strongly dependent on the intrinsic detector efficiency which should of course, be maximized. Calculations for a series of surface barrier detectors indicates that detector radius should be sacrificed to decrease detector noise.

The major source of background will be due to RTG gamma rays. Generally, the gamma ray background is 3 to 10 times more intense than the cosmic ray background but the specific ratio is dependent on detector type and geometry. Shielding on the order of 1 to 2 g/cm^2 of lead should be employed to reduce RTG background. It is expected that shadow shielding will be sufficient, however, the effect of air scattering in the Martian atmosphere must be evaluated to insure that it does not negate the effect of

TABLE 1-1

DETECTOR ANALYSIS SUMMARY

With exception of Scintillation Detector all data based on:[1]

(a) 1 cm detector radius, 3 cm^2 area
(b) 0.6 cm detector separation
(c) 1 cc dead volume in system
(d) Net geometric efficiency = $(V/V_T) \cdot \epsilon_g(h) = 0.635 \cdot (0.64) = 0.418$

Detector Type	Intrinsic Efficiency	β Reflection Coefficient	Counting Efficiency[2]	Background Rates[3] Cosmic Ray[5]	RTG Gamma[6]	Detector Thickness	Lead Shielding	Pu He Re
Thin Window, Pancake	0.365[7]	-	0.153	800 cpm	2,760 cpm	0.6 cm	1 g/cm^2	No
Avalanche	0.33[8]	0.2[9]	0.138	347	1,270	50μ	1 g/cm^2	No
Surface Barrier	0.60 (13 Kev FWHM 12°C)	0.2[9]	0.201	322	843	100μ	1 g/cm^2	≥15 Ke
Diffused Junction	0.62 (12 Kev FWHM 12°C)	0.2[9]	0.207	322	843	100μ	1 g/cm^2	≥15 Ke
Scintillation Detector	0.60[10]	-	0.60	0	11,000 810	0.01 cm	0 1 g/cm^2	No No

Notes

(1) Detector radius and separation optimized using figure of merit and assuming intrinsic efficiency independent of radius

(2) Fraction of C^{14} decays in total gas volume, including dead volume, that will be counted by the pair of detectors

(3) Background count rates quoted for most probable detector parameters indicated in subsequent columns of data. Rates for other va parameters can be found in Tables 2-1 through 2-3.

(4) Minimum detectable C^{14} decay rate based on criterion $R_S = \sqrt{R_B}$ and detector counting efficiency. Data for other values of detect parameters in Tables 2-4 through 2-7.

(5) Based on isotropic cosmic ray flux of 4 protons/cm^2-sec. Solar flare protons not included in background count rate.

(6) RTG gamma ray background evaluated at 1 meter from 2400 thermal watt RTG.

(7) Window is 1/4 mil mylar, 80% open. Transmission data obtained from literature (J.D. Ludwick, RSI, 33, 1335, 1962) and include β reflection from window.

(8) Measured in hemispherical chamber. Gas activity calibrated with ionization gauge before measurement. Accuracy estimated ~ 10%.

(9) Measured with gas source of specified activity, but not verified by direct calibration. Reflection coefficient may be in error by ± 50%.

(10) Based on preliminary measurement using a solid source.

FOLDOUT FRAME

ector kness	Lead Shielding	Pulse Height Rejection	Minimum Detectable C^{14} Decay Rate[4]	Comments
cm	1 g/cm^2	No	390 dpm	(1) Ineffective detectors because of high background rates. (2) Pulse height rejection not practicable. (3) Mylar and Kapton windows are permeable to water vapor.
)μ	1 g/cm^2	No	292	(1) Pulse height discrimination probably not effective in avalanche mode because of non-uniform gain. (2) Still developmental. (3) GE has tested a 3 cm^2 device complete with gold flashing RTV & Epoxy for 300 hrs @ 135°C and performance has improved slightly. (4) Not affected by water vapor. (5) Test results based on 1 cm^2 devices, 3 cm^2 devices are being investigated by GE.
00μ	1 g/cm^2	≥150 Kev	170	(1) Water vapor noise problem should be re-evaluated. (2) Less reliable than other semiconductor detectors from standpoint of noise stability. (3) Sterilizability not verified - have withstood 48 hours at 135°C - Goddard, D. Kling. (4) Generally less rugged than diffused junction type detectors.
00μ	1 g/cm^2	≥150 Kev	165	(1) Have passed heat sterilization tests at JPL, R. Wengert. (2) Noise level in larger detectors uncertain. (3) Front surface dead layer potential problem. (4) Lowest noise obtained with guard ring operation which requires active face to be operated at ~ +200 V. This may generate noise in the presence of saturated water vapor.
cm	0	No	170	(1) High efficiency and good background rejection. (2) Sterilizable and rugged. (3) Larger and heavier than internal gas counter. (4) CO_2 retention a possible problem.
	1 g/cm^2	No	50	

of radius

ors

ta. Rates for other values of

other values of detector

unt rate.

335, 1962) and includes

Accuracy estimated

may be in error by

a shadow shield. The shields should be placed as near to the RTG as practicable to minimize buildup. The gamma ray background can also be minimized by decreasing the thickness of the depletion layer, but the effectiveness of pulse height rejection of gamma rays will also be reduced when the depletion layer is less than about 100μ. The breadboard experiments will help define the optimum depletion layer thickness.

It is assumed that experiments will not be conducted during periods of intense solar flares, however, available data on solar flare intensity indicates that the background rate in semiconductor detectors during a storm will be comparable to the RTG gamma ray background. The detector performance would therefore not be seriously degraded, although it would of course be perferable to avoid solar flares.

Preliminary experiments and analysis of the plastic scintillation detector are very encouraging. The outer guard scintillator should be capable of rejecting virtually all the cosmic ray and solar flare background while both pulse height and coincidence rejection should effectively reduce the RTG gamma ray background in the inner scintillator. The design also provides 4π solid angle efficiency for detection of C^{14} beta particles. Moisture, dust and other contaminants, a critical problem with internal gas counters, should have relatively little effect on the scintillation detector. Potential problem areas with the detector are the adsorption of C^{14} in the plastic scintillator and its rather large physical size since it will require the use of two phototubes. It is possible that one of the photomultiplier tubes can be eliminated by employing pulse shape discrimination. Flight qualification of photomultiplier tubes should not be a problem.

1.3 RECOMMENDATIONS

It is recommended that diffused junction detectors be utilized in the Task II breadboard. This recommendation is based on a combination of several factors in which ruggedness and dependability have been weighed more heavily than ultimate sensitivity; namely

1. The available data on diffused junction detectors (which is meager) indicate that selected 1 cm^2 detectors can be made with a noise tail ending at 30 Kev. Larger detectors with a 3 cm^2 area have been made with a 55 Kev noise tail.

2. The diffused junction detectors have been shown to be sterilizable and are a much more rugged device than surface barrier detectors.

3. The surface barrier detectors are known to become very noisy when exposed to saturated water vapor and therefore are unlikely to be useful in the life detection experiments.

4. The avalanche detectors are being breadboarded in the Viking Life Detection Program and the results of that evaluation will be available to, and incorporated in, this C^{14} detector study.

5. Lithium drift detectors would be difficult to sterilize without damaging the detector and they cannot be operated at elevated temperatures.

The plastic scintillation detector should also be breadboarded in the Task II analysis. This novel design may prove to be a very effective detector for the Category C experiment.

During the Task II breadboard evaluation, the experiments should be designed to obtain information on the following parameters which have been difficult to evaluate in the Task I analysis.

1) Effect of depletion layer thickness on pulse height rejection efficiency for RTG gamma ray background.

2) The probability that a single gamma ray will produce coincident counts in the detector pair.

3) The absolute C^{14} detection efficiency as a function of discriminator level, which will be dependent on the amount of beta ray scattering from the detector and housing and on the dead layer thickness.

4) The effectiveness of lead shielding in reducing RTG gamma ray background. The effect of air scattering should be considered in these experiments.

5) The light collection efficiency in the scintillation detector and its dependence on the length of the counting volume.

6) Gamma ray rejection efficiency in the scintillation detector.

7) CO_2 retention by the detectors.

1.4 ANALYSIS PROCEDURES

The Task I analysis is reported in more detail in the subsequent sections of this report. The results of the paired detector evaluation for the Category A and B experiments is presented in Section 2. The preliminary experimental data and analysis of the scintillation detector for Category C experiment is presented in Section 3. The background radiation intensities employed in the calculation are discussed in Section 4. The procedures employed in calculating signal and background count rates for the paired detectors are then discussed in Section 5, 6, and 7. Section 8 contains a discussion of the figure of merit, $R_S/\sqrt{R_B}$, which was used to compare the effectiveness of the various types of detectors.

SECTION 2

EVALUATION OF DETECTOR PERFORMANCE FOR CATEGORY A AND B EXPERIMENTS

The key factors which distinguish the category A and B experiments from the pyrolysis part of the CO_2 fixation experiment are the following:

1) The total gas volume in the CO_2 Evolution and the Dark Release experiments is small compared to the 20 cc which must be counted in the pyrolysis experiment.

2) The positive flow nature of the pyrolysis experiment allows an opportunity to filter the gas and remove contaminants and at the same time fill a gas counter to a controlled pressure.

Hence the high sensitivity for a large sample which may be acheived with a gas fill proportional counter is not as necessary and would be made more difficult to implement for the first two experiment categories than for the last. The internal gas counter also imposes a weight and volume penalty particularly if some sort of anti-coincidence counter is to be included.

For these reasons the detectors considered for the CO_2 Evolution and Dark Release experiments are pairs of: (1) pancake proportional (geiger) counters, (2) surface barrier detectors, totally or partially depleted, (3) avalanche detectors, and (4) diffused junction detectors. The detector pairs are positioned in a face-to-face configuration and the evolved $C^{14}O_2$ gas is permitted to diffuse into the sensitive region between the detectors. This geometry provides increased solid angle efficiency, the opportunity to reduce background using anti-coincidence techniques and a measure of redundancy as a guard against detector failure. These same arguments apply to a tetragonal array of detectors, and even to the extreme of a spherical array, but the required electronic complexity becomes prohibitive. In view of the overall weight limitations imposed on the life detection package coupled with the large advantage a detector pair offers over a single detector, the number of detector elements per detector chamber was fixed at two. Once the performance is established for this case, extension to other geometries is

readily achieved. Ionization chambers were explicitly excluded on the grounds of poor sensitivity and because fast pulse counting as opposed to sensitive current measurements required by ionization chambers permits anti-coincidence rejection of cosmic rays and some gamma rays.

The results of the evaluation are summarized below. The procedures employed in generating the data are described in Section 4 through 8.

2.1 FIGURE OF MERIT

The criterion adopted for evaluating detector performance is the figure of merit, $R_s/\sqrt{R_B}$, where R_s is the C^{14} signal count rate and R_B is the background count rate. Detector performance is optimized when this figure of merit is maximized. The discussion in Section 8 shows that the figure of merit optimizes detector performance both with respect to detection accuracy and to the probability of detection. It also establishes a convenient criterion for the minimum detectable signal rate, namely

$$\text{Minimum Detectable } R_s = \sqrt{R_B} \text{ (in CPM)} \qquad (1)$$

This detection criterion is based on a counting time of 1 hour each for background and signal plus packground, and will result in a detection accuracy, σ/R_s, of 25%. The resulting probabilities for a false positive (i.e., unusually high background count being interpreted as a C^{14} signal) and false negative (i.e., unusually low signal count resulting in failure to identify a valid C^{14} signal) measurement are each equal to 3×10^{-3}.

2.2 OPTIMIZATION OF GEOMETRY

The figure of merit was employed to determine the optimum counting geometry. Since the background is proportional to the area of the detector face, it is convenient to equate $\sqrt{R_B}$ to the detector radius, R. The figure of merit then becomes

$$\frac{R_s}{\sqrt{R_B}} = \left(\frac{\epsilon_g(h)\,\epsilon_I}{R}\right)\left(\frac{\pi R^3 h}{\pi R^3 h + V_D}\right) \qquad (2)$$

where

$\epsilon_g(h)$ is the geometric or solid angle efficiency factor associated with the detector pair

ϵ_I is the intrinsic detector efficiency, i.e., fraction of betas incident on the detector face that are counted

h is the scaled separation distance between the detector pair (h = separation/R)

V_D is the "dead volume" in the detection system; i.e., any piping valves etc. $\pi R^3 h$ is the volume of gas located between the two detectors.

The equation for the figure of merit should also be multiplied by the C^{14} decay rate in the sample gas but since it is a multiplicative constant for all detector types, it is not included in the figure of merit calculation. The figure of merit was evaluated for dead volumes of 1, 3, and 5 cm^3, assuming the intrinsic efficiency is not dependent on detector radius. The results presented in Figure 2-1 show that the optimum configuration for a 1 cc dead volume is R = 1.0 cm and h = 0.6.

2.3 PERFORMANCE DATA

Background count rates due to RTG gammas and cosmic rays were then evaluated for each type of detector pair in the optimum configuration for 1 cc dead volume. The evaluation was done for a 1 cc dead volume since this represents the soil chamber size which will satisfy the requirement of the current science definition. The procedures employed in making these background estimates are described in a subsequent section of this report. The results obtained for a pair of pancake detectors are presented in Table 2-1 where detector thickness is the distance from the window to the back wall. The background rate data for solid-state detectors are presented in Table 2-2 (for cosmic ray background) and Table 2-3 (for RTG gammas). In these calculations the total RTG flux given in the Ames Research Center Spec. No. 15358 was scaled to 2400 thermal watts, but current information from Martin is that the number of RTGs have been reduced from four to two. The omnidirectional cosmic ray flux was taken to be 4 protons/cm^2-sec. The RTG gamma background rates given for solid-state detectors do not include pulse height rejection. With pulse height rejection, the background can be reduced to about 1/3 of the tabulated values as discussed in Section 7.2.

The background count rate data were used to calculate the minimum detectable C^{14} decay rate N, based on the equation

$$N = \left[\epsilon_g(h) \cdot \left(\frac{V}{V + V_D} \right) \cdot \epsilon_I \right]^{-1} R_s \qquad (3)$$

where R_s is the minimum detectable signal rate. From Equation (1), the minimum detectable signal rate, R_s, is

$$R_s = \sqrt{R_B} \text{ (in CPM)}$$

Figure 2-1 Geometry Optimization Curves

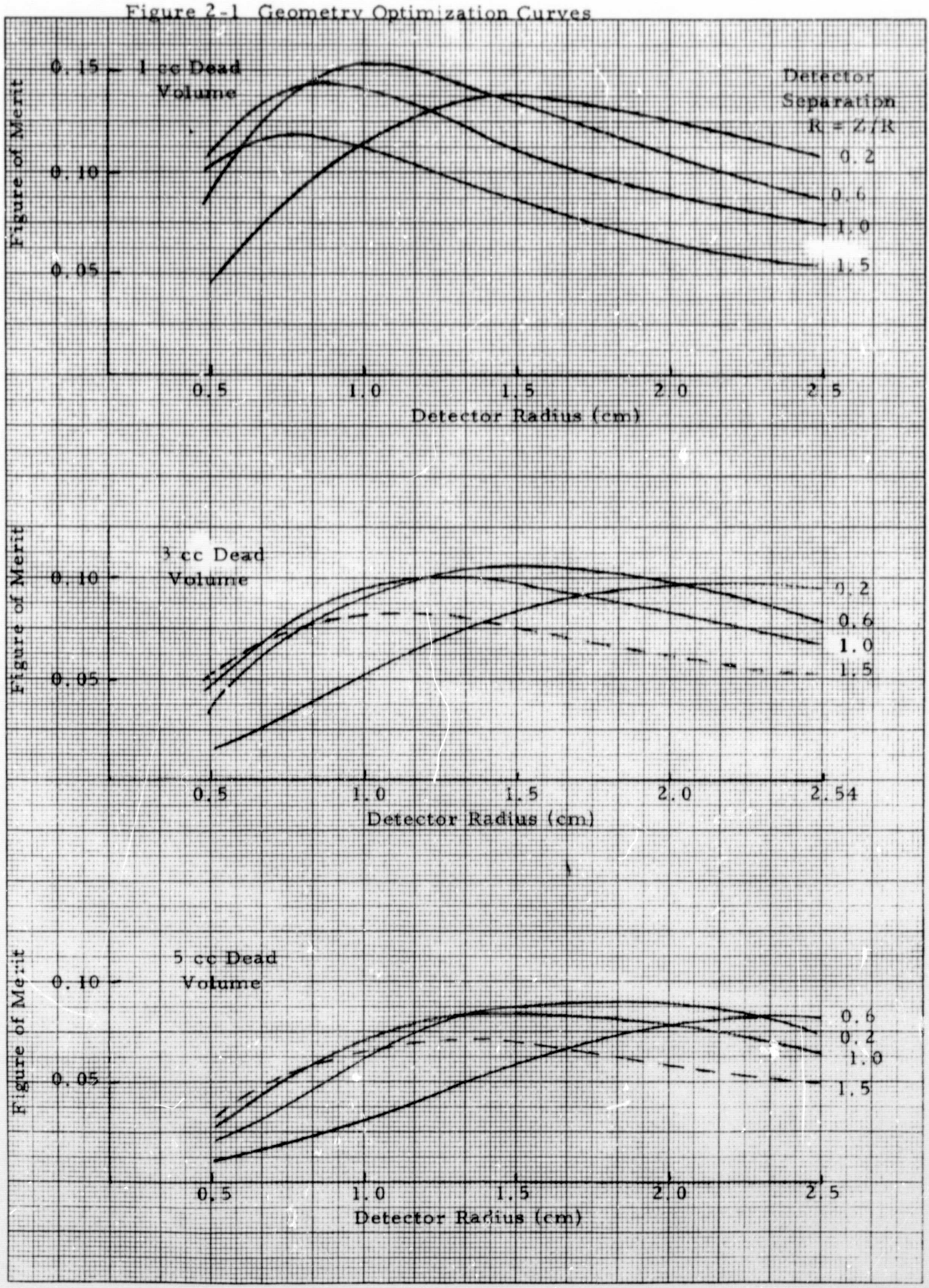

where R_B is the background count rate. If the signal rate and background rate are each measured for one hour, then this criterion results in about a 3×10^{-3} probability of a false negative or a false positive measurement. It also corresponds to a percentage error, σ/R_s, of about 25%. The results of the minimum detectable C^{14} decay rate calculations are tabulated in Tables 2-4 through 2-7, for proportional counters, avalanche detectors, surface barrier detectors, and diffused junction detectors, respectively. Selected results are presented in Figure 2-2. The intrinsic efficiency for the pancake detector was taken to be 0.365, based on published experimental data.[1] For the surface barrier and diffused junction detectors the values used were 0.48 and 0.49, respectively. These are based on a discriminator setting at 2.5 *FWHM at 10°C and include a 20% loss due to reflection of betas from the detector surface. Information on the noise of $3cm^2$ diffused junction detectors was not available so it was assumed that a selected detector could be found which would have the same relative noise as a surface barrier detector based on a comparison of $1cm^2$ diffused junction and surface barrier detectors. The intrinsic efficiency of the avalanche detector is 0.33, based on experimental data.

Calculations of optimum detector configuration were also made for a series of ORTEC partially depleted, surface barrier detectors in which ϵ_I varies as a function of detector radius (area). The characteristics of the detectors considered are summarized in Table 2-8. The results of the optimization procedure are presented in Figure 2-3. The top figure shows detector optimization vs detector radius with detector separation, h, as a parameter. The same data are replotted in the bottom figure vs detector separation h with detector radius (area) as a parameter. The results are suprising in that pairs of very small detectors can be made to have the same overall detection efficiency as larger area detectors. This is due to their lower noise which results in a higher intrinsic efficiency, ϵ_I. With larger dead volumes, the geometry inefficiency associated with small area detectors would be greater. This would reduce their overall efficiency and their efficiency relative to the larger detectors.

[1] J. D. Ludwick, RSI, 33, 1335 (1962)

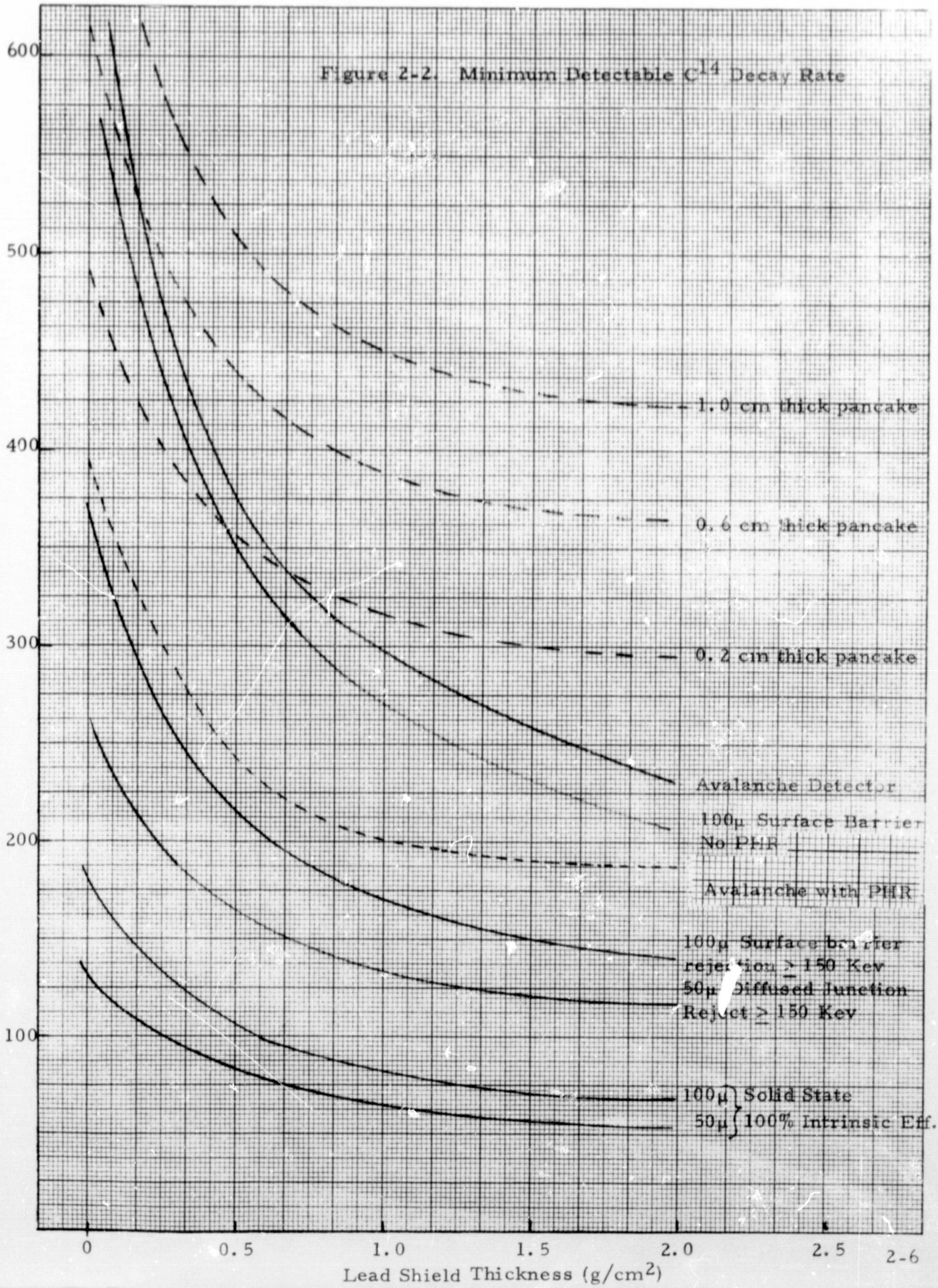
Figure 2-2. Minimum Detectable C^{14} Decay Rate
Minimum Detectable C^{14} DPM
600
500
400
300
200
100
1.0 cm thick pancake
0.6 cm thick pancake
0.2 cm thick pancake
Avalanche Detector
100μ Surface Barrier
No PHR
Avalanche with PHR
100μ Surface barrier
rejection ≥ 150 Kev
50μ Diffused Junction
Reject ≥ 150 Kev
100μ } Solid State
50μ } 100% Intrinsic Eff.
0
0.5
1.0
1.5
2.0
2.5
Lead Shield Thickness (g/cm²)

Figure 2-3 Optimization for Partially Depleted Surface Barrier Detectors

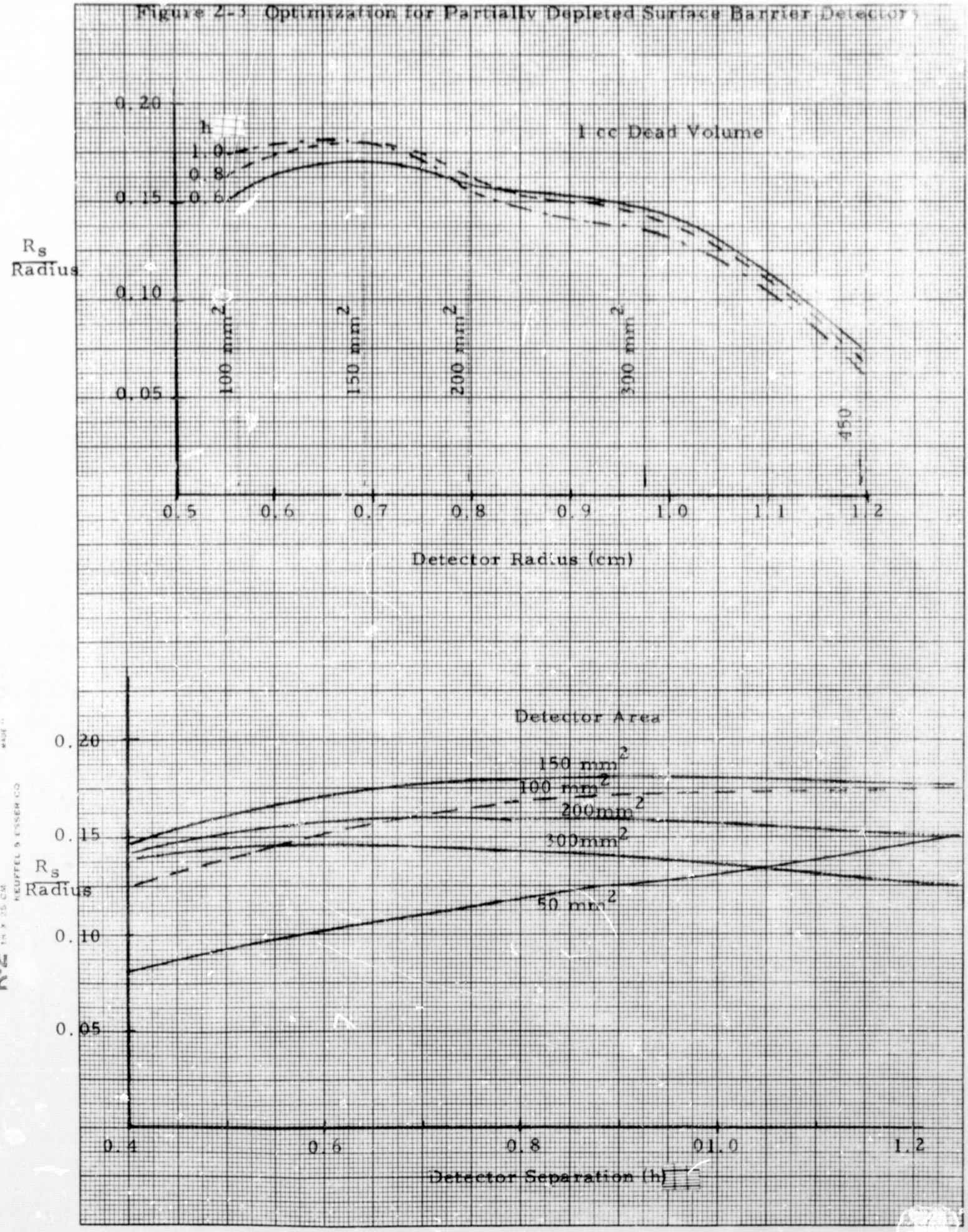

TABLE 2-1

BACKGROUND COUNT RATES IN THIN WINDOW PANCAKE COUNTER *

Thickness	Cosmic Rays (after coinc.)	RTG Gammas vs Lead Shield Thickness 0 g/cm^2	0.5	1.0	2.0
0.2 cm	498 cpm	5,260 cpm	2,410	1,635	1,510
0.4	650	6,580	3,010	2,290	1,880
0.6	800	7,910	3,620	2,760	2,260
1.0	1,100	10,500	4,820	3,670	3,050

*No pulse height rejection
Source scaled to 2400 Thermal Watts

TABLE 2-2

COSMIC RAY BACKGROUND RATES IN SILICON SOLID STATE DETECTORS

Depletion Thickness	No Pulse Height Reject. *	Pulse Height Rejection Above 150 Kev	125 Kev	100 Kev
50μ	347 cpm	333	338	341
100	347	322	312	292
150	347	291	267	222
200	347	248	205	125
300	347	125	26	0
C14 Beta Loss from Upper Level Discrimination		0 %	1.5%	8%

*Lower level set at zero
These rates are after coincidence.

TABLE 2-3

RTG GAMMA BACKGROUND RATES IN SILICON SOLID STATE DETECTORS**

Depletion Thickness	Gamma Background in counts per minute for Indicated Shielding* 0 g/cm^2	0.5 g/cm^2	1.0	2.0	4.0
50μ	7,650	2,260	1,270	660	375
100	15,300	4,510	2,540	1,320	750
150	22,900	6,750	3,800	1,970	1,120
200	30,500	9,000	5,070	2,620	1,490
300	45,800	13,500	7,610	3,940	2,250

*2400 Thermal Watts

**No pulse height rejection or anticoincidence rejection of gamma rays is considered. Pulse height rejection will reduce the gamma count rate to approximately 1/3 of the tabulated values. Some small rejection of gammas by coincident detection of the recoil electrons will be obtained, for instance, some 20% of the cobalt-60 1.3 Mev gammas give coincident counts in a pair of avalanche detectors arranged face-to-face 0.5 cm apart.

TABLE 2-4

"MINIMUM" DETECTABLE C^{14} DECAY RATE WITH PAIR OF THIN WINDOW PANCAKE COUNTERS

Detector Thickness	Lead Shielding 0 g/cm^2	0.5 g/cm^2	1.0	2.0
0.2 cm	495 dpm	353	316	292
0.4	556	396	354	329
0.6	610	435	390	362
1.0	704	503	451	421

TABLE 2-5

"MINIMUM" DETECTABLE C^{14} DECAY RATE WITH PAIR OF AVALANCHE DETECTORS*

Pb Shielding	0 g/cm^2	0.5	1.0	2.0	4.0
No Pulse Height Rejection	658 dpm	370	292	228	195
$\geq$150 Kev Rejection	390	240	200	172	157

*Sensitive region of detector taken to be 50 microns thick.

TABLE 2-6

"MINIMUM" DETECTABLE C^{14} DECAY RATE WITH PAIR OF SURFACE BARRIER DETECTORS

	Depletion Depth	Lead Shielding 0 g/cm^2	0.5	1.0	2.0	4.0
No Pulse	50μ	445 dpm	254	201	157	134
Height	100	622	347	268	203	165
Rejection	150	757	420	320	240	191
	200	871	482	367	271	213
	300	1,070	585	445	325	254
Pulse	50μ	268 dpm	165	138	118	108
Height	100	367	213	170	138	119
Rejection	150	443	251	197	154	129
≥150 Kev	200	510	284	219	167	136
	300	620	338	257	189	147

TABLE 2-7

"MINIMUM" DETECTABLE C^{14} DECAY RATE WITH PAIR OF DIFFUSED JUNCTION DETECTORS

	Depletion Depth	Minimum Detectable Decay Rate for Indicated Shielding				
		0 g/cm^2	0.5	1.0	2.0	4.0
No Pulse	50μ	431 dpm	246	194	152	130
Height	100	603	336	259	197	160
Rejection	150	734	407	310	232	185
	200	843	467	355	263	207
	300	1,035	567	430	315	246
Pulse	50μ	259 dpm	160	133	114	104
Rejection	100	355	206	165	133	115
$\geq$ 150 Kev	150	429	243	190	149	124
	200	493	275	212	162	132
	300	600	328	249	183	143

The evaluation of detector types for the CO_2 Evolution Experiment and the Dark Release Experiment indicates that solid state detectors will be more effective than the thin window pancake type gas counters. The fundamental reason for this is the poor transmission of the window coupled with the fact that a large fraction of the counter surface area is available to interact with the gamma rays but is not directly involved in the detection of the C^{14} betas. The larger volume is also more sensitive to the cosmic ray background. On the other hand the entire active area of the semiconductor detectors is sensitive to the betas. This results in the higher figure of merit evidenced by the solid state detectors. For given detector radius and depletion layers thickness, all solid-state detectors would have the same background count rates. Therefore, the important parameter of the solid-state detector is its intrinsic efficiency, and the dependence of the intrinsic efficiency on detector geometry as shown in Figure 2-3.

The choice of solid state detector to be breadboarded doesn't necessarily reflect a final choice for the life detection hardware, but is an effort to supplement experimental results being obtained with other promising detectors under the Life Detection Contract, NAS 25321. The side by side comparison should provide sufficient information to make a final selection among currently available detectors. Since the avalanche detector is presently under test the breadboard detector must be either a diffused junction detector or a surface barrier detector.

Since the weight, size and electronic complexity of these types of detectors is identical and the sensitivity to the radiation background will be the same for both, the choice must rest upon physical ruggedness, sterilizability, and intrinsic efficiency. Selected diffused junction detectors have approximately the same noise characteristics as commercially available surface barrier detectors. Selected surface barrier detectors will almost always have a lower noise than a comparable diffused junction detector. Surface barrier detectors will also have a thinner dead layer.

If it weren't for the fact that they are considerably less rugged, extremely sensitive to surface contamination and have not been proven sterilizable, the surface barrier detector would be selected over the diffused junction detector. Since dependability is considered paramount to ultimate sensitivity, the diffused junction detector has been selected for the task II breadboard.

TABLE 2-8

CHARACTERISTICS OF ORTEC PARTIALLY DEPLETED SURFACE BARRIER DETECTORS

Detector Area	FWHM (Betas)*	Detector Radius	Intrinsic Efficiency**
50 mm^2	13 Kev	0.46 cm	60%
100	15	0.56	53
150	17	0.69	48
200	20	0.80	40
300	22	0.98	35
450	30	1.2	18

*At 22°C

**The intrinsic efficiency listed here is the percent of the C^{14} beta energy spectrum above 2.5 times FWHM beta resolution and does not allow for betas backscattered from the detector.

2.4 COMPARISON WITH EXPERIMENTAL DATA

Experimental data on RTG background count rates in various types of detectors have become available subsequent to the completion of the Task I analysis[1]. A summary of the data is presented below and compared with the calculated results in order to assess the general validity of the analysis.

The experimental data verify the basic conclusion of the analysis, namely, that semiconductor detectors are preferable to thin window pancake detectors. The experimental data also indicate that lead shielding on the RTG is not very effective in reducing the background count rate. However, a large fraction of the count rates observed with a lead shadow shield in place appear to be due to air and room scattering. Therefore, the data probably do not accurately predict the effectiveness of lead as a shielding material or of the value of a shadow shield in the thin Martian atmosphere. Similarly, pulse height rejection of background in semiconductor detectors was found to be less effective than estimated but these results may also be influenced by the scattered radiation.

2.4.1 Comparison of Total Background Count Rates

Background count rates produced by a SNAP-27 fuel capsule were measured for two types of geiger tubes and for 3 types of semiconductor detectors. The measured count rate in the two geiger tubes is presented in Table 2-9 which also summarizes the physical characteristics of the two tubes employed in the experiments. To facilitate later comparison with calculated results, the measured background is also expressed in units of count rate per unit area of detector wall surface. The fact that the normalized count rate in both detectors are nearly equal indicates that it is valid to assume that the background count rate is proportional to the total wall area, as was done in the calculations. The higher normalized count rate in the EON 6213 tube is probably attributable to the thicker counter wall which makes it more sensitive to high energy gamma rays.

Background count rate data for the three semiconductor detectors are presented in Table 2-10. The quoted values for background have been

---

[1] "RTG/Science Instrument Radiations Interactions Study for Deep Space Probes", NAS 2-5222, by TRW Systems Group, Redondo Beach, California, 1969, CR 73360.

TABLE 2-9

MEASURED RTG BACKGROUND IN GEIGER TUBES

Tube Type	EON 6213	EON 7302
Dimensions[1]:		
ID	0.093"	7/16"
Length	0.30"	1/4"
Wall	0.125"SS	0.020"SS
Measured Background[2]	15 counts/sec at 3 ft	57 counts/sec at 3 ft
Background rate per unit area of wall surface	1.38×10^3 $\frac{\text{Counts}}{\text{cm}^2\text{-min at 3 ft}}$	1.2×10^3 $\frac{\text{Counts}}{\text{cm}^2\text{-min at 3 ft}}$

[1] From EON Corporation detector catalog.

[2] "RTG/Science Instrument Radiations Interactions Study for Deep Space Probes", NAS 2-5222, by TRW Systems Group, Redondo Beach, California, 1969.

extracted from pulse height distributions curves found in the TRW report. For comparison with calculated values, the experimental data are expressed in units of counts/min per cm^2 of detector area per μ of depletion layer thickness. The normalized count rates for all three detectors are roughly equal. Since the depletion layer thicknesses range from 53 to 500 microns, the assumption that the total count rate is proportional to the thickness of the depletion layer is also justified, at least as a first approximation.

It is difficult to make direct comparisons of the experimental and calculated background data because of differences in the RTG source spectra and intensity and in the specific detector characteristics. A relative comparison can be made by calculating the ratio of the normalized count rates quoted above to the corresponding values obtained in this study. Values of this ratio are tabulated in Table 2-11 for each of the detectors employed in the experiments. The ratio is, in effect, the ratio of measured count rate to the count rate that would be predicted using the computational techniques employed in this study. However, the normalized count rates have not been adjusted for differences in source intensity, etc, so the absolute values of the ratio have no special significance.

Comparison of the data in Table 2-11 shows that the ratios obtained for the geiger tubes are about 2 to 4 times larger than the ratios for the semiconductor detectors. Therefore, the experimental data indicate that the estimates of background in geiger tubes or pancake detectors are 2 to 4 times less than they should be, in comparison to the estimates of background in the semiconductor detectors. Thus, the performance of pancake detectors will be even poorer than predicted in the analysis and the conclusion that semiconductor detectors are preferred over pancake detectors is justified.

2.4.2 Effectiveness of Lead Shielding

Experimental data are reported on the effectivensss of lead shielding in reducing RTG background rates. The measurements were made using a flat sheet of lead (2 ft x 2 ft) as a shadow shield, placed adjacent to the detector. The results of the shielding experiments for the geiger tubes and a 2mm x 0.8 cm^2 lithium-drifted semiconductor detector are presented in Figure 2-4. For comparison, the predicted attenuation curves for the RTG spectrum and total attenuation curves for monoenergetic gamma rays of 100, 200, 500, and 1,000 Kev are also included in the figure.

TABLE 2-10

MEASURED RTG BACKGROUND IN SEMICONDUCTOR DETECTORS[1]

Detector:			
Type	Surface Barrier	Surface Barrier	Lithium Drift
Thickness	53μ	200μ	500μ
Area	1 cm^2	1 cm^2	0.8 cm^2
FWHM	35 Kev (for alpha)	24 Kev (for alpha)	13 Kev (for Beta)
Measured Background:			
Total Counts (>50 Kev) at 3 ft.	825 c/min	4,630 c/min	5,750 c/min*
Counts in 50 to 150 Kev Window at 3 ft	770 c/min	3,390 c/min	3,280 c/min*
Normalized Rates:		"Counts/Min-cm^2-μ"	
Total (>50 Kev)	15.6	23.1	14.4*
50 to 150 Kev	14.5	16.9	8.2*

[1] From TRW Study

*Lower level discriminator for the lithium drift detector was set at 75 Kev rather than 50 Kev.

TABLE 2-11

COMPARISON OF EXPERIMENTAL AND CALCULATED RTG BACKGROUND COUNT RATES

	Ratio of Measured to Predicted Count Rates[1]	
A) Geiger Tubes:		
EON6213	7.90	
EON7302	6.85	
B) Semiconductor Detectors	Total Count >50 Kev	Window Count 50 to 150 Kev
53μ, 1 cm^2	1.93	5.05
200μ, 1 cm^2	2.85	5.90
500μ, 1 cm^2	1.78[2]	2.86[2]

[1]The ratio of observed to predicted counts does not account for differences in source intensity, etc. Therefore, only the relative values of the ratio should be compared; the absolute value of the ratio has no special significance.

[2]Lower level discriminator for experimental data set at 75 Kev rather than 50 Kev.

The experimental data indicate that shielding is not very effective in reducing the background. However, the data appear to be unreliable, probably because of air and room scattering. For example, the experimental results show that lead shielding will be more effective with geiger tubes than with semiconductor detectors. This result is questionable because: (1) the gamma ray detection efficiency in a semiconductor detector is very high at low energies and decreases monotionally with increasing gamma energy; whereas, the efficiency of a geiger tube is small at low energies and tends to increase with gamma ray energy, (2) most of the gamma ray flux from the RTG is emitted at low energies ($\leq$300 Kev) where lead has a strong photoelectric absorption cross section, and (3) in the Mev range where the geiger tube efficiency is maximum, the attenuation coefficient in lead is small and predominately Compton scattering. Therefore, lead shielding should be more effective in reducing the count rate in a semiconductor detector then in a geiger tube, contrary to the experimental data.

The observed result is perhaps due to air and room scattering around the lead shadow shield employed in the experiments. The hypothesis of scattered radiation is consistent with the experimental data in that the scattered radiation will have lower energies than the primary flux and therefore is more likely to be detected with the semiconductor detector. Thus, air scattering around the shadow shield would make the shield appear less effective for the semiconductor detectors than for the geiger tubes. This does not rule out the use of shadow shields with the C^{14} detectors because scattering will be much less important in the tenuous atmosphere of Mars but some additional shadow shielding may also be needed to reduce ground scatter radiation.

If scattered photons make a significant contribution to observed count rates, then the background ratios discussed in the preceeding section would be even more strongly biased against geiger tubes.

2.4.3 Pulse Height Rejection of Background

The data in Table 2-10 indicate that pulse height rejection in thick semiconductor detectors will reduce the count rate to $\sim$75% of the count observed without rejection. This is considerably less effective then the estimated value of 33%. Although the estimated rejection efficiency is not considered to be very reliable, part of the discrepancy between the estimate and the experimental value may be due to the scattering problem discussed above.

Figure 2-4 Lead Shielding Effectiveness

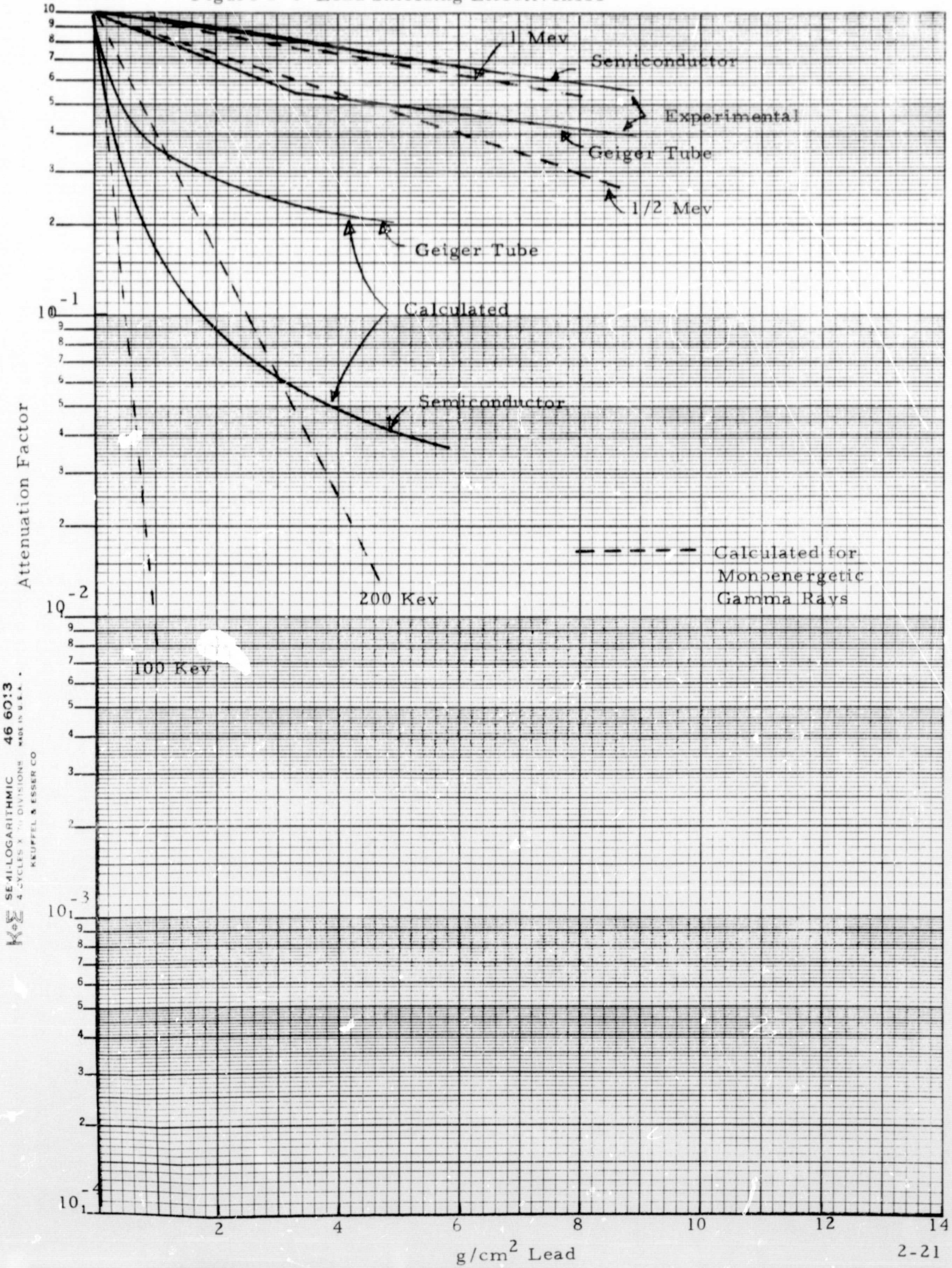

2.4.4 Coincidence Rejection of Background

Experimental data are also reported on the background coincidence rate in a semiconductor telescope. These experiments were conducted with a 2000μ x 0.8 cm^2 lithium drift detector and a 200μ x 1 cm^2 surface barrier detector, spaced 0.47 cm apart. The output from the larger detector was fed through a linear gate into a pulse height analyzer. The thin detector, with a lower level discriminator set at 96 Kev, provided the gating signal for coincidence measurements made with a 1 μ sec resolving time.

The results of gamma background measurements made with the telescope arrangement are presented in Table 2-12. The pulse height distribution for coincidence events has almost the same shape as the "No Coincidence" distribution so the coincidence rate is not strongly dependent on photon energy.

TABLE 2-12

COINCIDENCE DATA FOR SEMICONDUCTOR TELESCOPE

Type of Count	Count Rate	Percent
No Coincidence Count Rate	776 cps	100
Anticoincidence Count Rate	736	95
Coincidence Count Rate	43	5.5
Accidental Coincidence Rate	0.5	0.06

A 5 percent reduction in background count rate was achieved with the specified telescope characteristics. The characteristics of the proposed C^{14} detectors will be considerably different from the experimental arrangement so the result is not directly applicable to the proposed system, however, the coincidence rejection efficiency should increase for several reasons.

First, the gate threshold in the C^{14} detectors will be set at about 30 Kev rather than the 96 Kev threshold employed in the experiment. The lower gate setting should result in a considerable increase in coincidence rate. The C^{14} detectors will also be considerably thinner than the telescope detectors. Both the total count rate and the coincidence rate will decrease with decreasing detector thickness but the total count rate should decrease at a faster rate. The percentage of coincidence events can therefore be expected to increase in the thinner C^{14} detectors. The coincidence rate is undoubtedly dependent on the separation of the detectors so this factor will also influence the coincidence rate. The experimental data therefore indicate that it will be possible to achieve at least a 5 percent reduction in RTG background by using coincidence rejection and the rejection efficiency for the C^{14} detectors may be considerably higher.

SECTION 3

SCINTILLATION DETECTOR

The double walled scintillation detector has been selected for breadboard evaluation in the Task II phase. Because of its large sensitive volume (20 cc), the detector is designed primarily for use with the Category C experiment although it could also be employed with the Category A and B experiments.

3.1 DETECTOR DESIGN

The unique feature of this detector which makes it attractive for the Category C experiment is the double scintillator construction with the 4π thin inner scintillator separated from the guard scintillator by a minimum of non-scintillating material. This construction serves two purposes: First, the gamma interaction rate in the inner scintillator is held to a minimum, and second, some fraction of the recoil electrons from those interactions which do occur will deposit sufficient energy in the outer scintillator to permit these events to be eliminated by an anti-coincidence requirement. In addition, gammas which interact in the outer scintillator and produce recoil electrons detected in the inner scintillator may be rejected in the same way. This design also provides a large volume 4π counting geometry for the C^{14} and a 4π anticoincidence shield which should virtually eliminate cosmic rays. The major drawback is the size of the device which would approach 6" in length and 3" in diameter using available ruggedized photomultipliers. For flight hardware, it might be possible to eliminate one of the phototubes by replacing the plastic guard scintillator with a CsI crystal and using pulse shape discrimination to distinguish between events in the two scintillators.

A drawing of the proposed scintillation detector is shown in Figure 3-1. In this breadboard design, both scintillators will be made of NE160 plastic which has good stability at high temperatures and will be capable of withstanding the sterilization cycle. The inner scintillator is 0.1 mm thick and the guard scintillator 8.2 mm thick. EMI 9635B phototubes will monitor scintillations in the two crystals; the inner plastic by a phototube mounted at the right face in the drawing and the outer plastic by a tube at the left face.

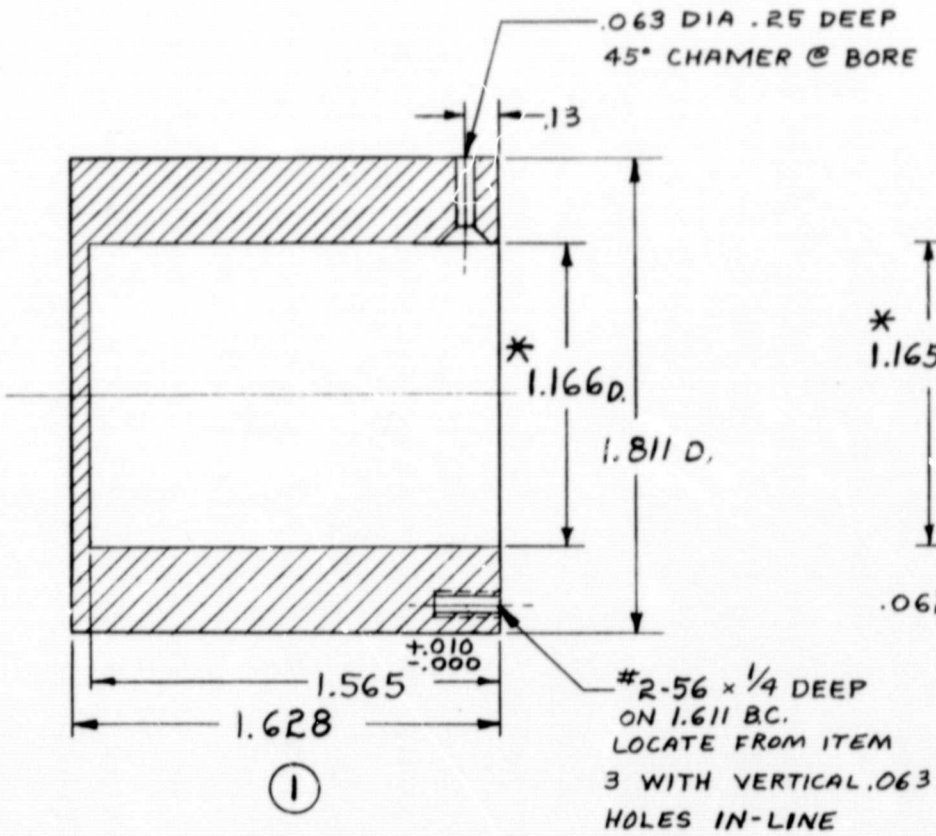

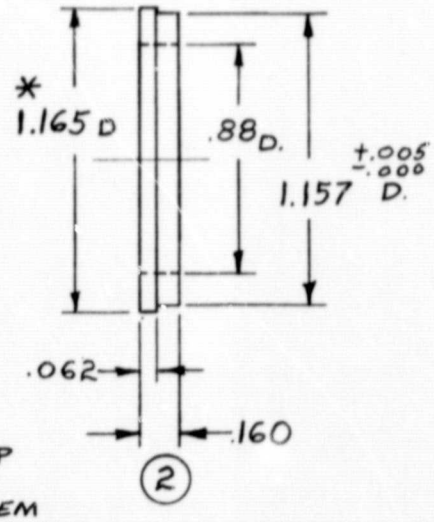

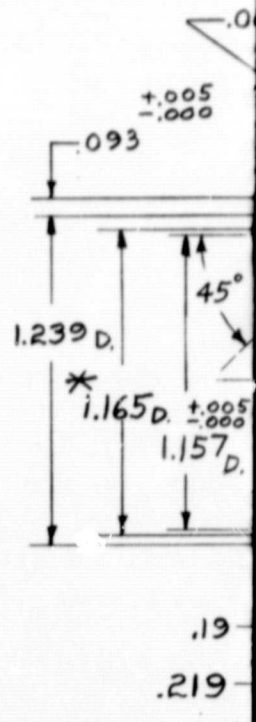

NOTES:

* 1. THE 1.165 DIA. ON ITEMS 2 & 3 TO BE APPROX. .008 LARGER THAN THE 1.157 +.005 -.000 DIA., TO BE FLUSH WHEN ITEM 5 ASSEMBLED. THE 1.166 DIA ON ITEM 1 TO ALLOW SLIP FIT AT ASSEMBLY.

2. MATERIAL: ITEMS 2 & 3 NON-SCINTILLATING NE-160
   " 4 NE 160 - 0.1 mm THK x 1.150 DIA ONE PART .090 HOLE @ ITEM 3
   " 5 NE 160 - 0.1 mm THK x 1.4
   " 1 NE 160
   " 6 PARKER "O" RING #2-26 (1/16 x 1 1/4 x 1 3/8)
   " 7 SS TUBING .062 DIA
   " 8 #2-56 x 3/8 LG RND. HD. SCREW (4)

3. PAINT OUTER SCINTILLATOR (ITEM 1) WITH REFLECTING PAINT ON OUTER DIA. ONLY. VACUUM DEPOSIT OPAQUE ALUM. COATING ON INSIDE AND EDGE WHERE SEALED TO ITEM 3.

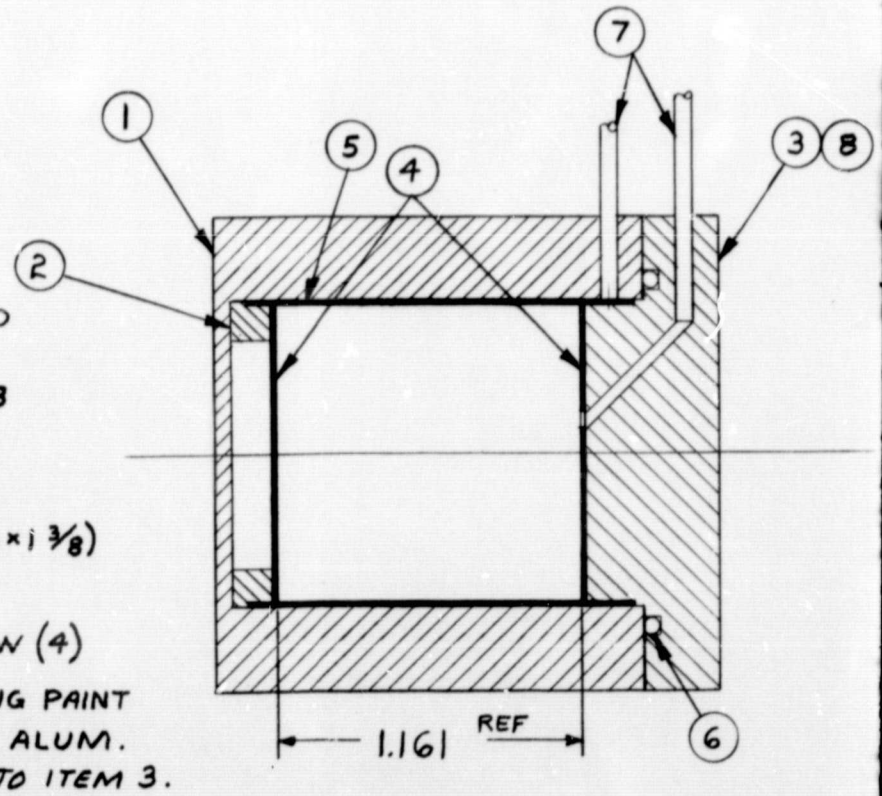

UNLESS OTHERWISE SPECIFIED: DIMENSIONS ARE IN INCHES TOLERANCES DECIMAL .X ± .XX ± .03 .XXX ± .005 ANGLES ± CHAMFER ± 5° SURFACE FINISH MICROINCHES RHR	CONTR NO.
MATERIAL: NOTE 1	DRAWN
	CHECKED
	STRESS/WT
	DSGN SUPV
	PROJ ENGR
	QUAL CONT
	SYS SPT
	DSGN APPL
	MFG
	CUSTOMER

X1	EXPERIMENTAL RELEASE ER 1695 —	9-12-69	J.H.J.
X2	REV PER ECN X2	9-17-69	J.H.J.

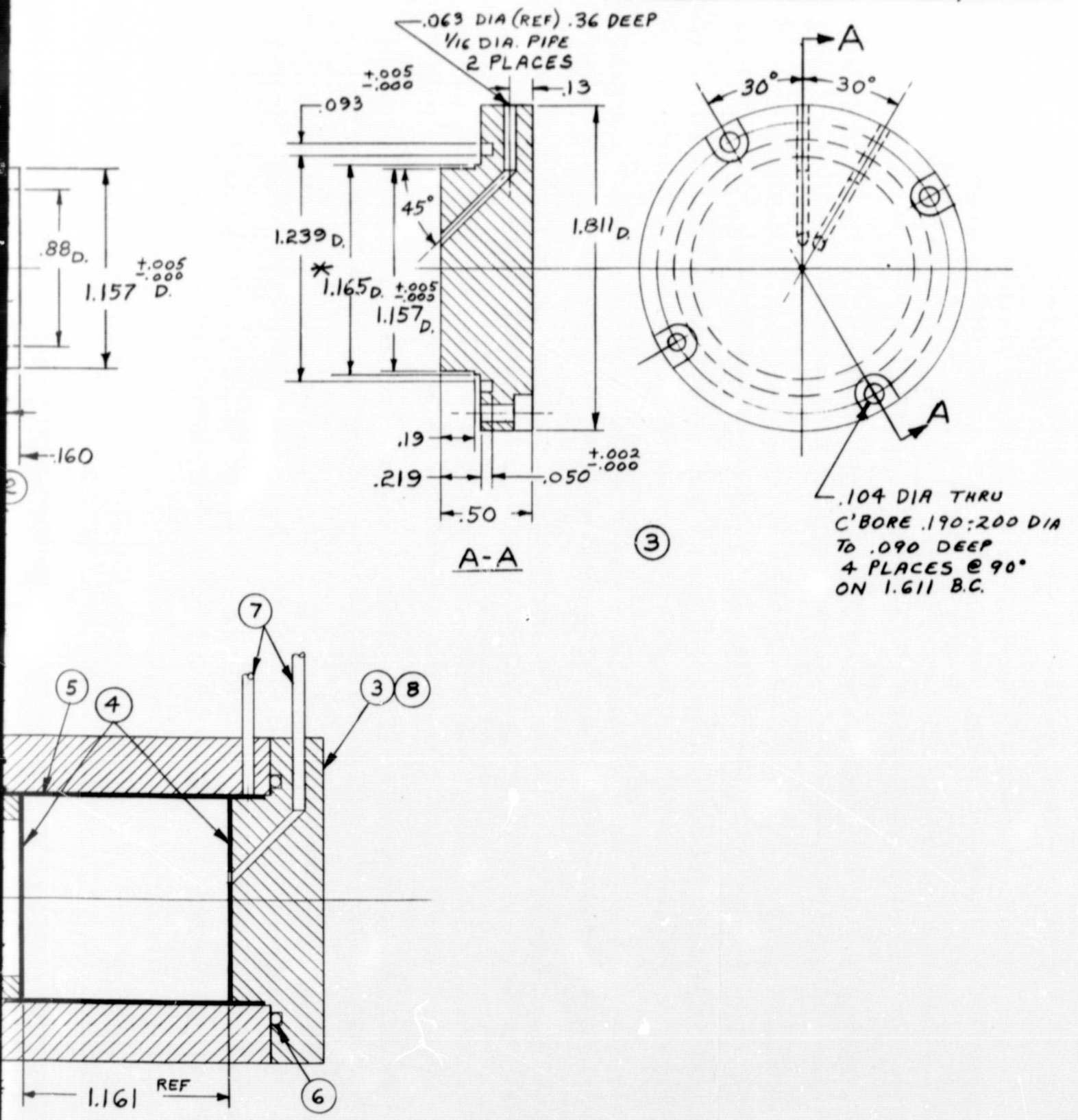

UNLESS OTHERWISE SPECIFIED:	CONTR NO.		
DIMENSIONS ARE IN INCHES	DRAWN	BKANICK	9/10/69
TOLERANCES	CHECKED	J Bamford	9/11/69
DECIMAL ANGLES	STRESS/WT		
.X ± ±	DSGN SUPV		
.XX ± .03	PROJ ENGR		
.XXX ± .005 CHAMFER ± 5°	QUAL CONT		
SURFACE FINISH	SYS SPT		
MICROINCHES RHR	DSGN APPL		
MATERIAL: NOTED	MFG		
	CUSTOMER		

THE BENDIX CORPORATION
AEROSPACE SYSTEMS DIVISION – ANN ARBOR, MICHIGAN

TITLE
SCINTILLATION
DETECTOR

SIZE	CODE IDENT NO.	DRAWING NUMBER	REV.
C	07038	BSX 9749	X2

SCALE 2/1 | WEIGHT | SHEET

FOLDOUT FRAME

In the breadboard design, the inner cylinder can be pulled out of the guard cylinder and replaced with alternate designs. It is hermetically sealed so that C^{14} gas cannot diffuse into the space between the two scintillators. Aluminum will be vacuum deposited on the inside surfaces of the guard cylinder to prevent light leaks between the two scintillators. Provision has been made for evacuating the space between the two scintillators to minimize pressure loadings on the inner plastic during the breadboard testing.

The EMI 9635B phototube selected for the breadboard detector is neither sterilizable nor miniature, but exhibits excellent signal-to-noise characteristics along with high gain. Several ruggedized tubes have superior performance to this tube but cost up to twenty times more. It is felt that the detector performance with the EMI 9635B tube can be extrapolated with sufficient accuracy so that the added expense is not justified in the breadboard design. Characteristics of three possible ruggedized tubes are compared with the breadboard item in Table 3-1.

The dimensions of the inner detector were obtained by minimizing the total surface area of the detector and making the total volume equal to about 20 cc so that it would have sufficient capacity for counting effluents from the gas chromatograph. If the C^{14} detection sensitivity is assumed to be independent of source position and account is taken of the fact that one end of the cylinder will not have a gamma guard, then the optimum ratio of radius to length is given by

$$r = \frac{\alpha}{1 + \alpha} h$$

where $1 - \alpha$ is the fraction of the gamma ray count rate, per unit surface, that can be eliminated by coincidence techniques. Sufficient data on rejection efficiency and detection sensitivity are not yet available so that the dimensions selected for the chamber volume might not be optimal. Measurements to be made during the Task II breadboard evaluation will permit optimization of the design.

TABLE 3-1

PHOTOTUBES SUITABLE FOR SCINTILLATION DETECTOR

Tube Type	Cathode	Cathode Sensitivity	Gain	Overall Sensitivity	General
EMI #9635B	1.7"dia. Sb K Cs	86.5 mA/watt at 4200 Å, peak at 3800 Å	2×10^6 at 1100 volts	160 A/L at 1100 volts with dark current 0.4 nA	Not ruggedized, not sterilizable, 6" long x 2" dia. Delivery from stock. $230.00
P 10 Johnston Labs.	2" dia. Sb K Na	61 mA/watt at 4200Å: peak at 4100Å	2×10^6 at 2150 volts	100 A/L at 2150 volts with dark current of 0.1 nA	Ruggedized and sterilizable 2" long x 3" dia. Focused mesh multiplier, 180 grams (6.4 oz) with divider. Delivery 4-6 weeks. $4950.00
541 U-01-14 EMR Photoelectric	1" dia. multialkali	79 mA/watt at 4200 Å, peak at 4100 Å	2×10^6 at 2800 volts	188 A/L at 2800 volts with dark current of 0.1 nA	Developed for Mars Lander under JPL Contract #95155 Sterilizable and ruggedized 4-1/2"long x 1.25"dia. 170 gram(6 oz) potted with divider 10 week delivery. $3000
8850 (Formerly C-31000D) RCA	1.8" dia. KCs Sb	93 mA/watt at 4200 Å peak at 3999 A	2×10^6 at 1825 volts	180 A/L at 1825 volts with dark current of 0.5 nA	Sterilizable Ruggedized 5.71" long x 2.1" dia. 6 oz. Delivery 4-6 weeks, $600

3.2 PRELIMINARY DATA

Measurements have been made to determine the C^{14} beta detection efficiency of the plastic scintillator. The data presented in Figure 3-2 show pulse height distributions obtained with a C^{14} point source located at three different positions along the length of the inner cylinder which was 2 inches long, 0.75 inches in diameter and 0.2 mm thick. The high count rates observed at small pulse heights are uncertain because of tube noise.

The data are replotted as integral spectra (counts greater than E) in Figure 3-3 which also shows the integrated noise spectrum. The curves show that source position has a marked influence on count rate at large pulse heights but, with a discriminator setting at the tube noise level around channel 10, the count rate is relatively insensitive to source position. The data indicate that the C^{14} detection efficiency with a discriminator level set at channel 10 is approximately 60 per cent. Other experiments have indicated that most of the light reaching the phototube travels directly through the gas chamber rather than being piped through the plastic. The scintillator thickness has therefore been reduced to 0.1 mm for the breadboard model. This will reduce the gamma sensitivity by 50 per cent with virtually no sacrifice in beta sensitivity.

Preliminary tests have also been made of gamma rejection efficiency with a guard crystal. The rejection efficiency for Cs^{137} gamma rays is approximately 50%. The rejection efficiency, however, is strongly dependent on threshold settings in the two detector circuits so additional testing will be required to determine rejection efficiency. Tests will also have to be made to determine if C^{14} retention in the plastic is a problem.

Figure 3-2 C^{14} Pulseheight Spectra with Scintillator

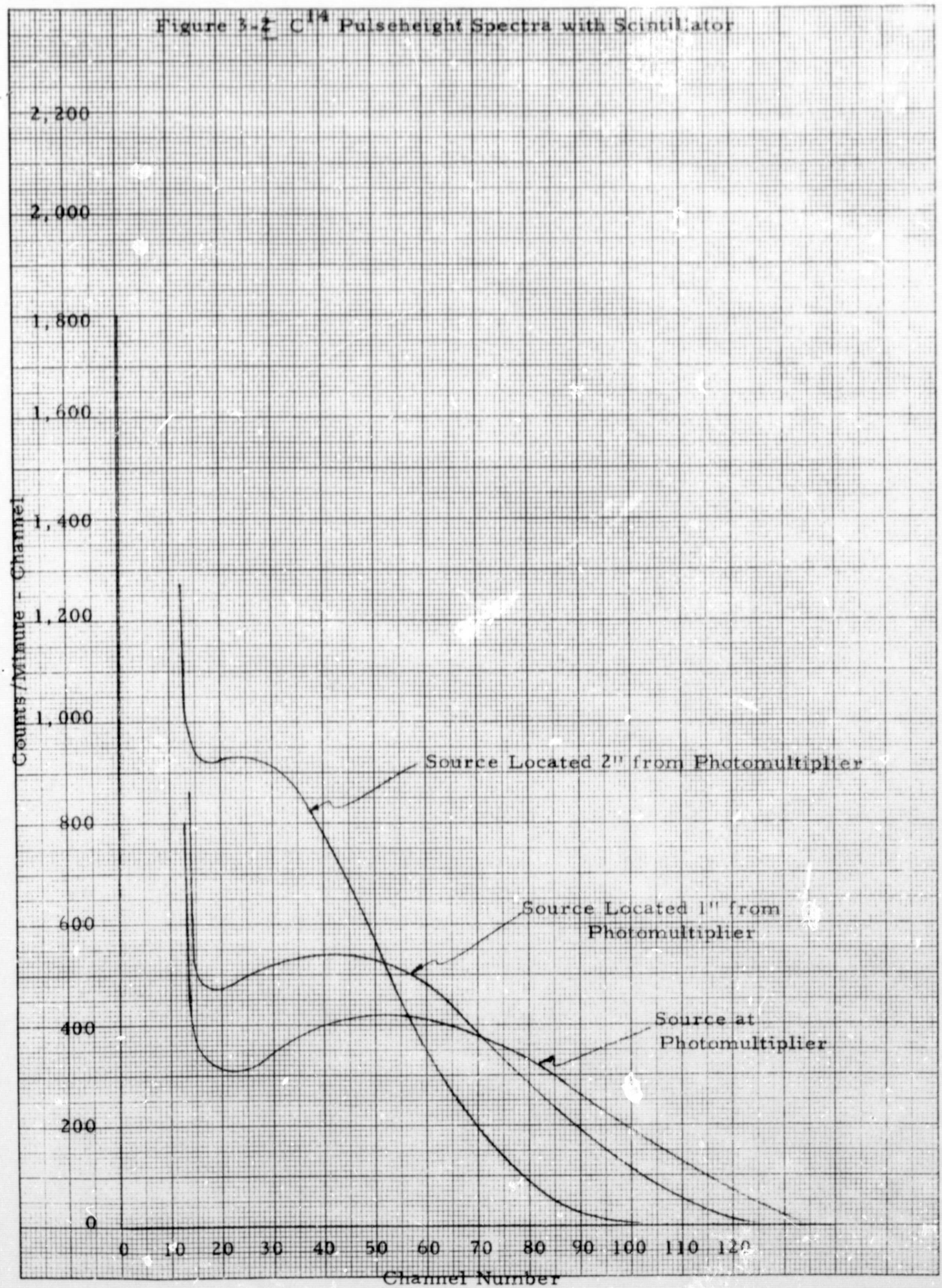

Figure 3-3 Integral Spectra for 3 Different C^{14} Source Locations

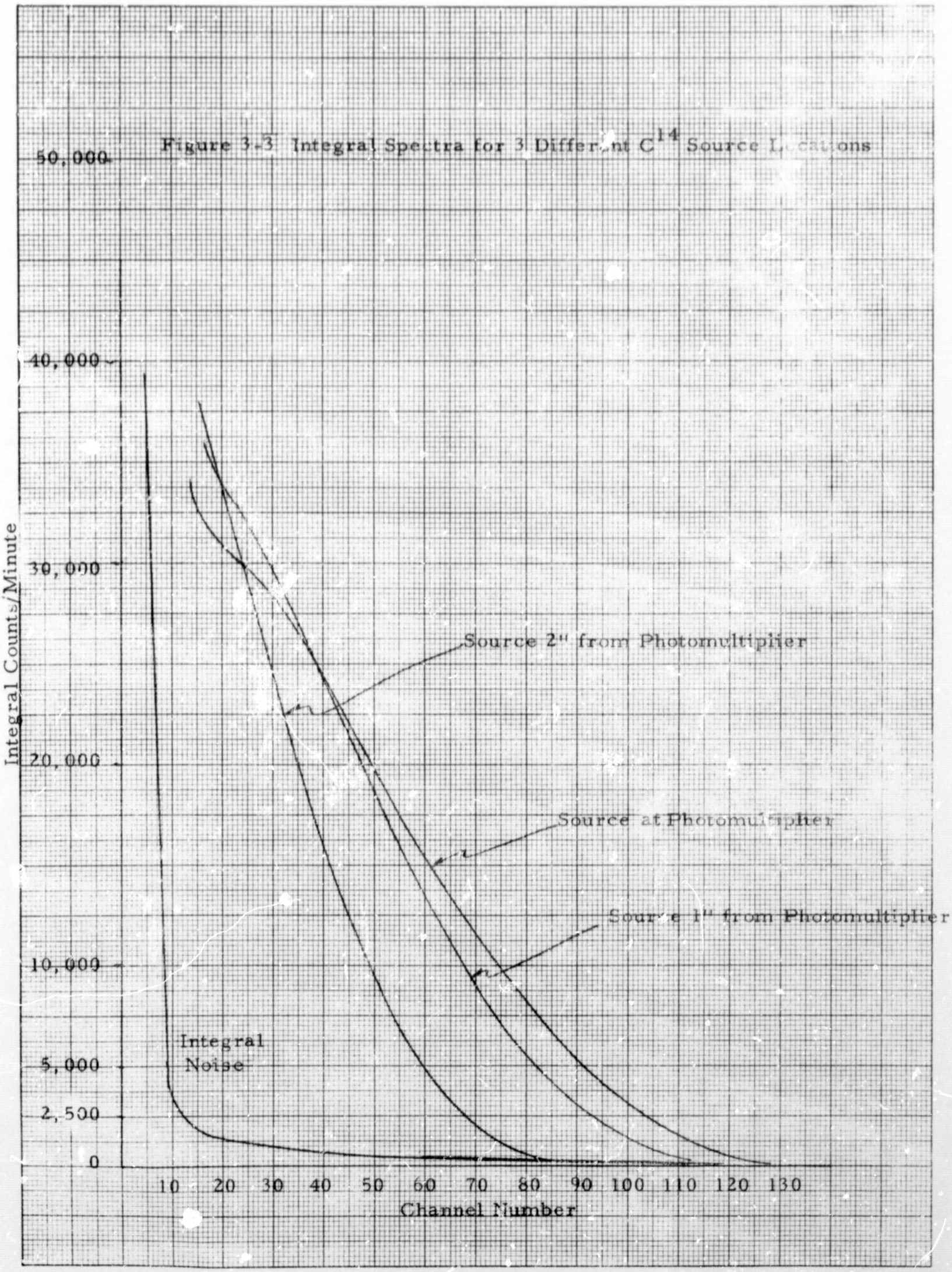

SECTION 4

C^{14} AND BACKGROUND SPECTRA AND INTENSITY

4.1 C^{14} SPECTRUM

The C^{14} beta ray differential energy spectrum employed in the calculations is presented in Figure 4-1. The figure also contains a plot of the integral spectrum for estimating counting efficiency dependence on discrimator level setting.

4.2 RTG GAMMA RAY AND NEUTRON SPECTRA

The RTG gamma ray spectrum employed in the calculations is presented in Table 4-1. The data are normalized to an RTG power output of 800 thermal watts so an additional factor of 3 must be introduced into the calculations to provide an effective RTG output power of 2400 thermal watts. The shape of the spectrum was obtained from data reported by the Martin Marietta Corporation.[1] The neutron spectra is presented in Table 4-2. The spectrum is also normalized to 800 watts. Neutron background count rates are very small compared to the gamma ray background so the neutron contribution is not included in estimates of the total background count rate.

4.3 COSMIC RAYS AND SOLAR FLARE PROTONS

For the purposes of the Task I analysis, the intensity of the cosmic ray flux at the Martian surface is taken to be 4 protons/cm^2-sec and the flux is assumed to be isotropic. There is some uncertainty in the value, but based on several different sources of data[2] and crude calculations, it should be accurate to within a factor of 2.

---

[1] "SNAP-19 Phase III Final Report" MND-3607-239-3, Martin Marietta Corporation, May 1968.

[2] "Mars Scientific Model" Document 606-1 by the Jet Propulsion Laboratories and "Mars Engineering Model, Viking Project" M73-106-0 by the Viking Project Office, NASA

Figure 4-1. Integral and Differential C^{14} Beta Spectrum

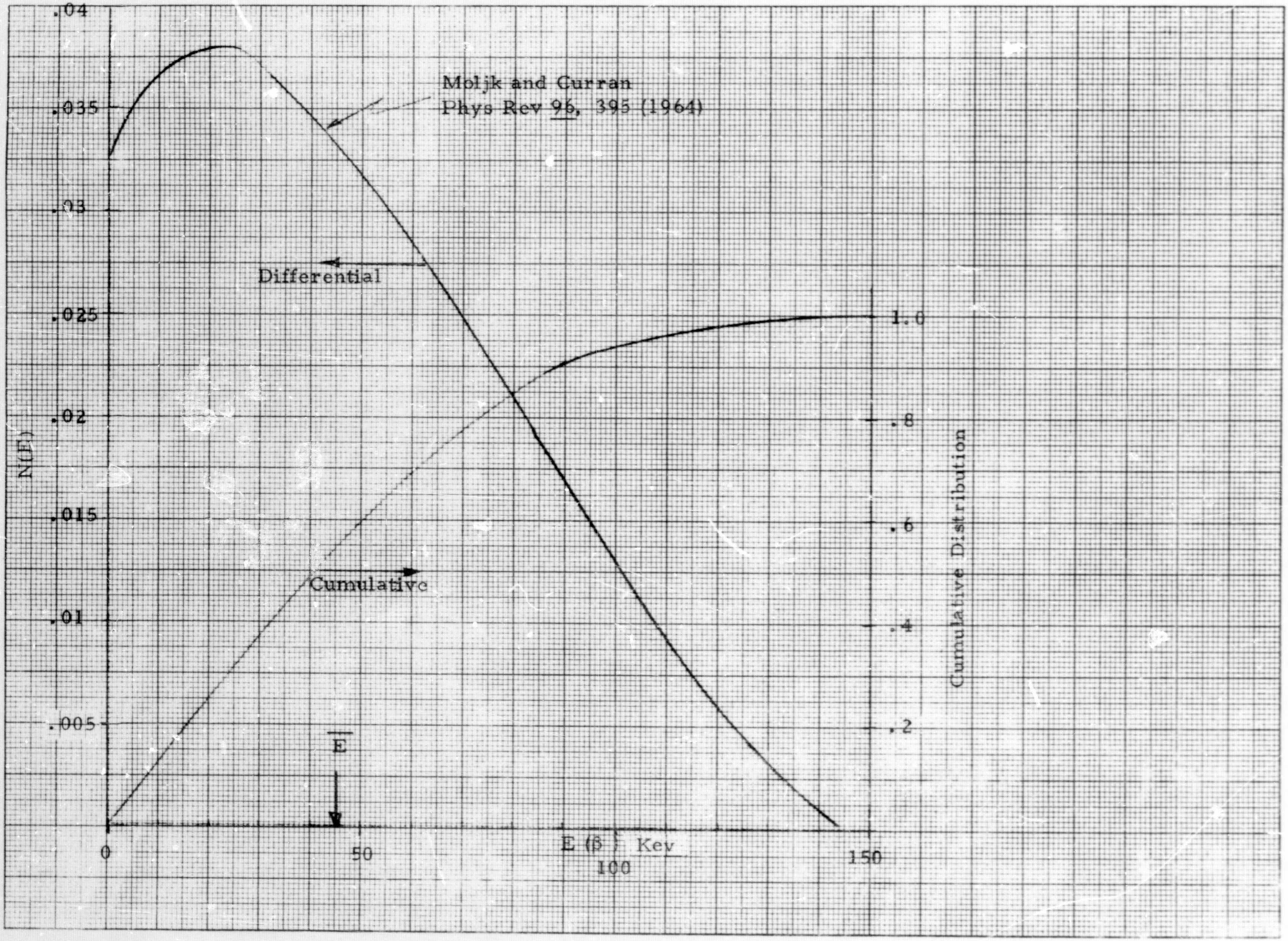

TABLE 4-1

RTG GAMMA RAY SPECTRUM (NORMALIZED TO 800 THERMAL WATTS)

Energy Group	Energy Interval	Gamma Ray Flux at 1 Meter
1	1.0 - 2.0 Mev	2.72×10^3 γ/cm^2-min
2	0.7 - 1.0	7.68×10^3
3	0.5 - 0.7	9.00×10^3
4	0.3 - 0.5	1.51×10^4
5	0.16 - 0.3	1.90×10^4
6	0.10 - 0.16	6.78×10^4
7	0.06 - 0.10	2.28×10^4
8	0.00 - 0.06	1.66×10^4

TABLE 4-2

RTG NEUTRON SPECTRUM

Neutron Energy	Neutron Flux
0.0 - 0.5 Mev	4.5×10^0 n/cm^2-sec at 1 meter
0.5 - 1.0	9.1×10^0
1.0 - 2.0	6.3×10^1
2.0 - 3.0	1.3×10^2
3.0 - 4.0	5.7×10^1
4.0 - 5.0	5.7×10^0
5.0 - 6.0	9.6×10^{-1}

Solar flare background has not been considered explicitly in the calculations because it is assumed that the experiments will be "turned off" during strong flares or the counting periods scheduled so as to avoid intense flares. Data available in the request for proposal and "Mars Engineering Model" M73-106-0 indicate that the peak proton flux (> 100 Mev)[1] during a severe solar flare would be ~15 to 30 protons/cm^2-sec. Based on background calculations made thus far, the RTG gamma ray background is considerably more intense than the cosmic ray background, so, a solar flare background of this magnitude would not have a serious effect on the performance of the detector system. However, the estimate of the solar flare flux appears to be unusually low in comparison to data for the free space flux. It should therefore be investigated more carefully before it is concluded that the life detection experiments can be conducted during a solar flare storm.

[1] For semiconductor detectors with depletion depths greater than ~ 100μ, only solar flare protons with energy greater than 100 Mev will contribute to the background count rate. Lower energy protons can be rejected with an upper level discriminator operating at 150 kev. Because of the guard crystal, solar flare protons will not be a serious problem with the plastic scintillation detector.

SECTION 5

C^{14} SIGNAL COUNT RATES

The procedures employed to calculate C^{14} signal rates in the pancake proportional counters and semiconductor detectors are described below.

5.1 SIGNAL RATE IN PAIR OF PANCAKE PROPORTIONAL COUNTERS

In the operational geometry, the two pancake detectors will be mounted face-to-face with the C^{14} and carrier gas positioned in the space between the detectors. The C^{14} count rate for the pair of detectors in this geometry is

$$\text{Signal Count Rate} = \epsilon_g(h) \cdot T_w \left[\frac{\pi R^3 h}{\pi R^3 h + V_D}\right] \cdot N \quad \text{Counts/min}$$

where $\epsilon_g(h)$ is the average solid angle collection factor for the sample volume

T_w is the window transmission factor for the detector. The window (1/4 mil mylar) is 80% open and the transmission probability for C^{14} betas was taken to be 0.456[1]. The net transmission factor is $T_w = 0.365$.

R is the radius of the pancake detector

h is the scaled detector separation, (i.e., h = linear separation/detector radius).

V_D is the dead volume in detector system

N is the number of C^{14} decays/min in gas sample

---

[1] Transmission probability calculated from data available in "High Geometry Gas Cell Proportional Counter" by J. D. Ludwick, RSI 33, (1962).

This procedure for estimating signal count rate is expected to be accurate to within ± 20 percent. The greatest uncertainty in the calculation is the window transmission factor. Since the value employed in the calculation is based on experimental data obtained in a similar counting geometry, it should be reliable.

5.2 SOLID STATE DETECTOR SIGNAL COUNT RATE

As with the pancake proportional counters, the solid state detectors are assumed to operate in pairs, face-to-face. The signal count rate is then

$$\text{Signal Count Rate} = \epsilon_g(h) \cdot \epsilon_I \cdot \left[\frac{\pi R^3 h}{\pi R^3 h + V_D}\right] \cdot N$$

where, as before,

$\epsilon_g(h)$	is the average solid angle collection factor for the sample volume
R	is the radius of the detector
h	is the scaled detector separation; separation/radius
V_D	is the dead volume in the detector system
N	is the number of C^{14} decays/min in the gas sample
ϵ_I	is the intrinsic detection efficiency of the detector; i.e., the fraction of C^{14} betas incident on the detector that produce a detector count.

The intrinsic efficiency for avalanche detectors (1/4" x 5/8" in size) was experimentally measured to be 0.33 for C^{14} betas. This value is considered to be reliable for the particular detector employed in the experiment and it is assumed that the same value would be obtained for other sizes of avalanche detectors.

For other types of solid state detectors, the intrinsic efficiency is determined by the FWHM of the detector noise level. A low level discriminator is set at 2.5 · FWHM. This setting, in conjunction with the

cumulative energy distribution of the C^{14} betas determines the maximum number of betas that could possibly be detected. This maximum possible detection efficiency is then multiplied by 0.8 to account for the reflection of beta particles from the detector surface. The 20% reflection probability is based on experimental data obtained with a surface barrier detector. However, the calibration of the C^{14} source activity is uncertain so the reflection coefficient may be in error by $\pm$ 20 percent. Otherwise, the calculation of the signal count rate for semiconductor detectors is considered to be reliable.

SECTION 6

COSMIC RAY BACKGROUND

Cosmic ray background count rates were obtained with the procedures described below.

6.1 TOTAL COUNT RATE

The total background count rate due to cosmic rays will be proportional to the number of cosmic ray particles that enter the sensitive volume of the detector. Since the cosmic ray flux, S protons/cm^2-sec, is assumed to be isotropic, the number of protons which will enter through a unit surface area is

$$\text{Number/area} = \frac{S}{4\pi} \int_{\Omega} \text{Cos}\ \theta \cdot d\Omega = S/4$$

The total cosmic ray count rate in the detector is therefore

$$\text{Cosmic Ray Count Rate} = S/4 \cdot \epsilon \cdot (\text{Surface Area})$$

where ϵ is the efficiency for detecting the cosmic ray protons which enter the detector and the "surface area" refers to the surface area of the sensitive volume of the detector (assumed to have convex shape).

6.2 COINCIDENCE RATE BETWEEN PAIRS OF DETECTORS

When a pair of detectors are operated in coincidence, a portion of the cosmic ray background can be rejected since some cosmic ray particles will trigger both detectors. The coincidence rate can be calculated by noting that the cosmic ray flux which passes through a differential area of the detector surface has a Lambertian distribution. The problem of calculating the coincidence rate between two detectors is therefore identical to the well documented problem of calculating radiative heat transfer between the two detectors. The coincidence rate is then

$$\text{Coincidence Rate} = S/4 \cdot A \cdot F \cdot 2$$

where, in analogy to radiative heat transfer,

$S/4$	is the energy radiated per unit area of detector
A	is the surface area of detector #1 that can be viewed by detector #2.
F	is the "view factor" associated with the area A; i.e., the fraction of energy radiated from area A on detector #1 that is intercepted by detector #2.

The additional factor of 2 is introduced because protons contributing to the coincidence rate can either enter or leave detector #1 through the area A. It is assumed the detector efficiency, ϵ, is unity; otherwise the equation must be multiplied by the factor ϵ^2.

As an example, consider a pair of cylindrical detectors of radius R and thickness T, mounted coaxially and separated a distance H. The total cosmic ray count rate in the pair of detectors is

$$\text{Total Count Rate} = 2 \cdot S/4 \cdot (2\pi R^2 + 2\pi RT)$$

The coincidence rate for the detector pair is

$$\text{Coincidence rate} = 2 \cdot S/4 \cdot \pi R^2 \cdot F_D,$$

where F_D is the view factor for two disks of radius R separated a distance H. Defining $t = T/R$, the net count rate in the detector pair, after subtraction of the coincidence count rate, is

$$\text{Net Cosmic Ray Count Rate} = S \cdot \pi R^2 \cdot (1 + t - F_D).$$

Plots of the net cosmic ray count rate vs. detector radius are presented in Figures 6-1 and 6-2 for various values of t and $h = H/R$.

Figure 6-1. Cosmic Ray Count Rate In Pair of Detectors of Zero Thickness, After Correcting for Coincidences Resulting From Detector Separation, h

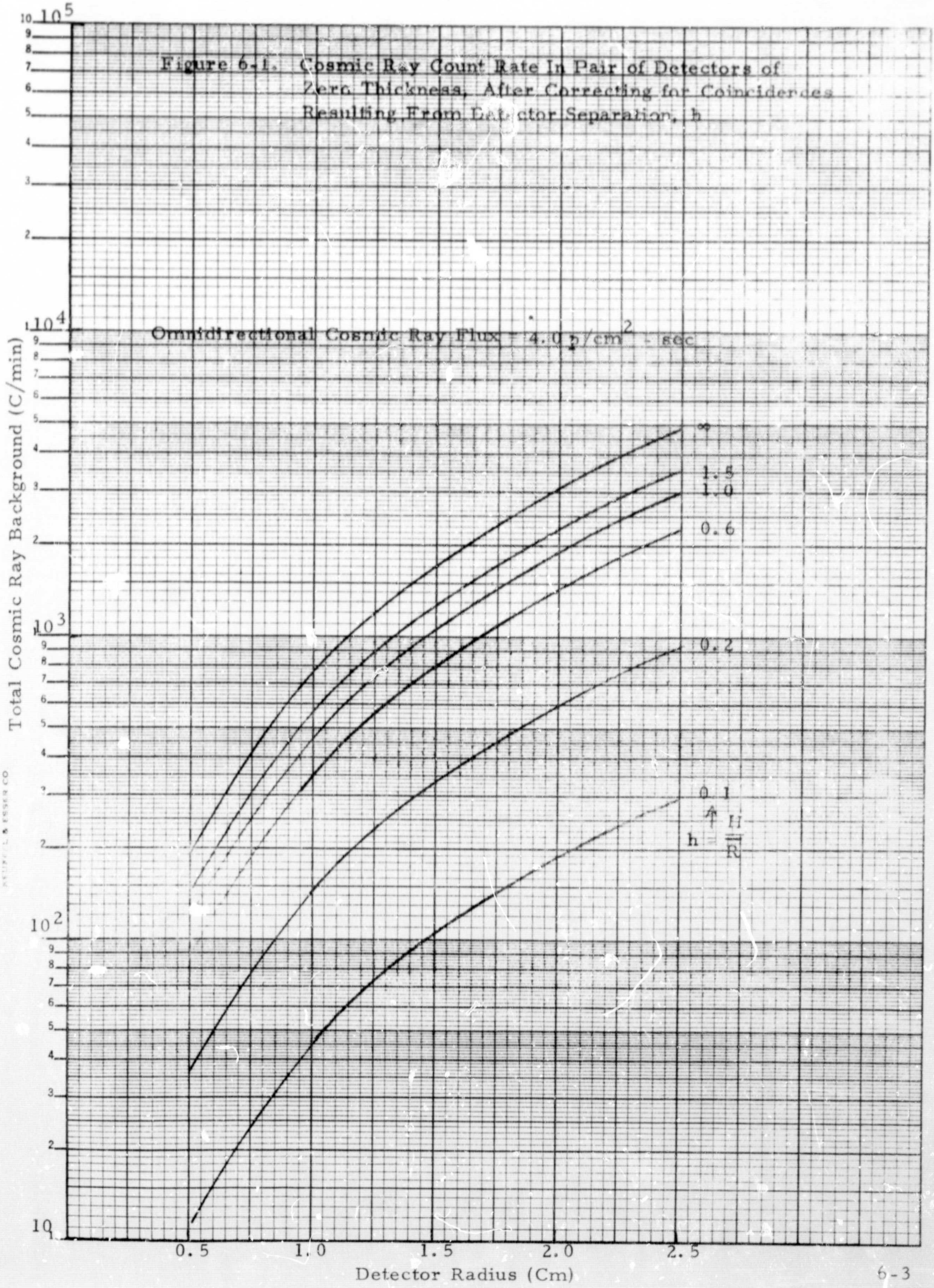

Figure 6-2. Cosmic Ray Count Rate In Pair of Pancake Detectors of Thickness t = 0.5R and also t = 1.0R; Corrected for Coincidence Counts Produced by Detector Separation

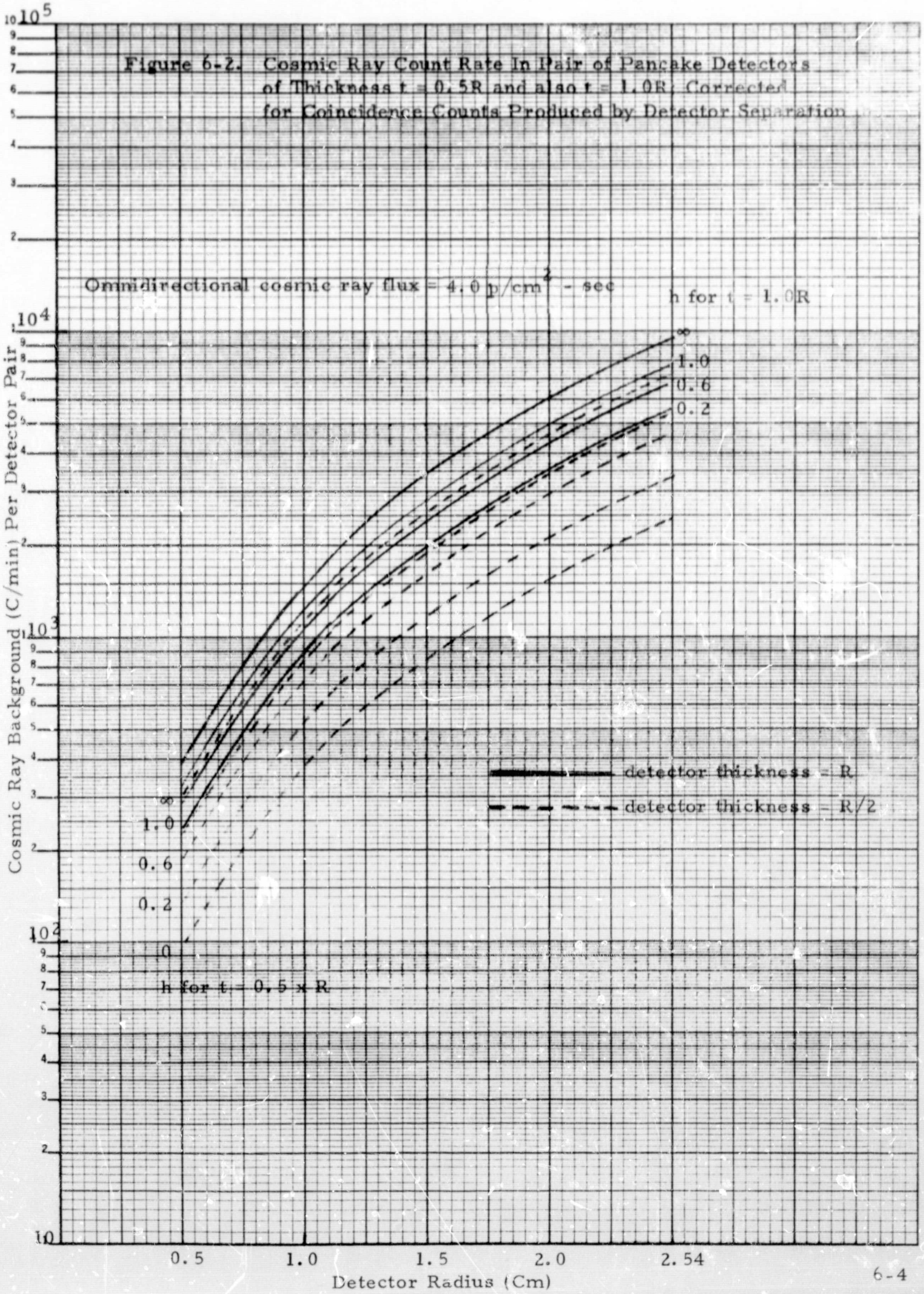

6.3 PULSE HEIGHT REJECTION OF COSMIC RAYS

The cosmic ray background can also be reduced by rejecting those cosmic ray events which deposit more than a specified amount of energy in the detector. To estimate the effectiveness of this rejection technique, it will be assumed that:

1) the detector is thin; i.e., a solid state detector*

2) the protons are minimum ionizing, 0.4 Kev/μ of silicon, and there is no fluctuation in the rate of energy loss

3) the flux is isotropic and the protons travel in straight lines.

Since the flux is isotropic, the probability that an incident cosmic ray will enter the detector at angle θ from the normal to the surface is

$$p(\theta) \cdot d\theta = 2 \cdot \text{Sin}\ \theta \cdot \text{Cos}\ \theta \cdot d\theta$$

If the depletion layer is t microns thick, a proton entering at the angle θ will travel a distance $\lambda = t/\cos\theta$ in the detector and the corresponding energy deposition, E, will be

$$E = 0.4t/\text{Cos}\ \theta$$

The probability q(E) of observing an energy loss E can therefore be obtained by equating the probability distributions

$$q(E)\,dE = p(\theta) \cdot d\theta = p(\theta) \cdot \frac{d\theta}{dE} \cdot dE$$

$$= 2 \cdot \xi^2 \cdot (dE/E^3)$$

where $\xi = 0.4 \cdot t$ is the energy that would be deposited by a vertically incident proton. The fraction, Q(E), of incident protons that deposit more than the energy E is

$$Q(E) = \int_E^\infty q(E) \cdot dE = (\xi/E)^2$$

Thus, the fraction of cosmic ray events retained after pulse height rejection is

*Pulse height rejection does not appear to be practicable in a "thick" pancake proportional counter. See Section 7.1.2.

2

$$\text{Fraction Retained} = 1 - (\xi/E)^2$$

Where E is the energy (Kev) of the upper level discriminator, $\xi = 0.4 \cdot t$ is the energy (Kev) deposited by a vertically incident proton and t is the depletion layer thickness in microns.

For a 100μ depletion layer and discriminator setting of 100 Kev, the fraction of counts retained is

$$1 - \left(\frac{40}{100}\right)^2 = 0.84.$$

Graphs of the fraction of cosmic rays retained as a function of discriminator level setting are presented in Figure 6-3 for several thicknesses of the depletion layer. The fraction of the C^{14} beta spectrum that would be rejected as a function of the discriminator setting is also shown in the Figure. The curve for the C^{14} betas is only the integral of the energy distribution. It does not account for the angular distribution of incident beta particles so the fraction rejected is overestimated.

6.4 VALIDITY OF CALCULATIONS

There are uncertainties in the cosmic ray calculations; namely:

1) intensity of the cosmic ray flux (4 p/cm^2-sec) which may be in error by a factor of 2

2) assumption of isotropy which may be invalid; particularly if "massive" objects are positioned assymetrically "near" the detectors, also if both pulse height rejection and coincidence rejection are used, the cosmic rays which traverse the counters making small angles with the normal will tend to be rejected by the anticoincidence requirement so that the average energy deposited by the remaining particles will be somewhat higher making pulseheight rejection more efficient than indicated.

3) calculations of pulse height rejection should account for fluctuations in energy loss.

Generally, the accuracy of the calculation of cosmic ray background is believed to be more reliable than the calculations of the RTG gamma ray background. The present calculations also indicate that the cosmic ray

Figure 6-3. Pulse Height Distribution Produced by Isotropic Flux of Minimum Ionizing Particles:

$$\left(\frac{dE}{X}\right)_{min} \approx 0.4 \text{ Kev}/\mu \text{ M Si}$$

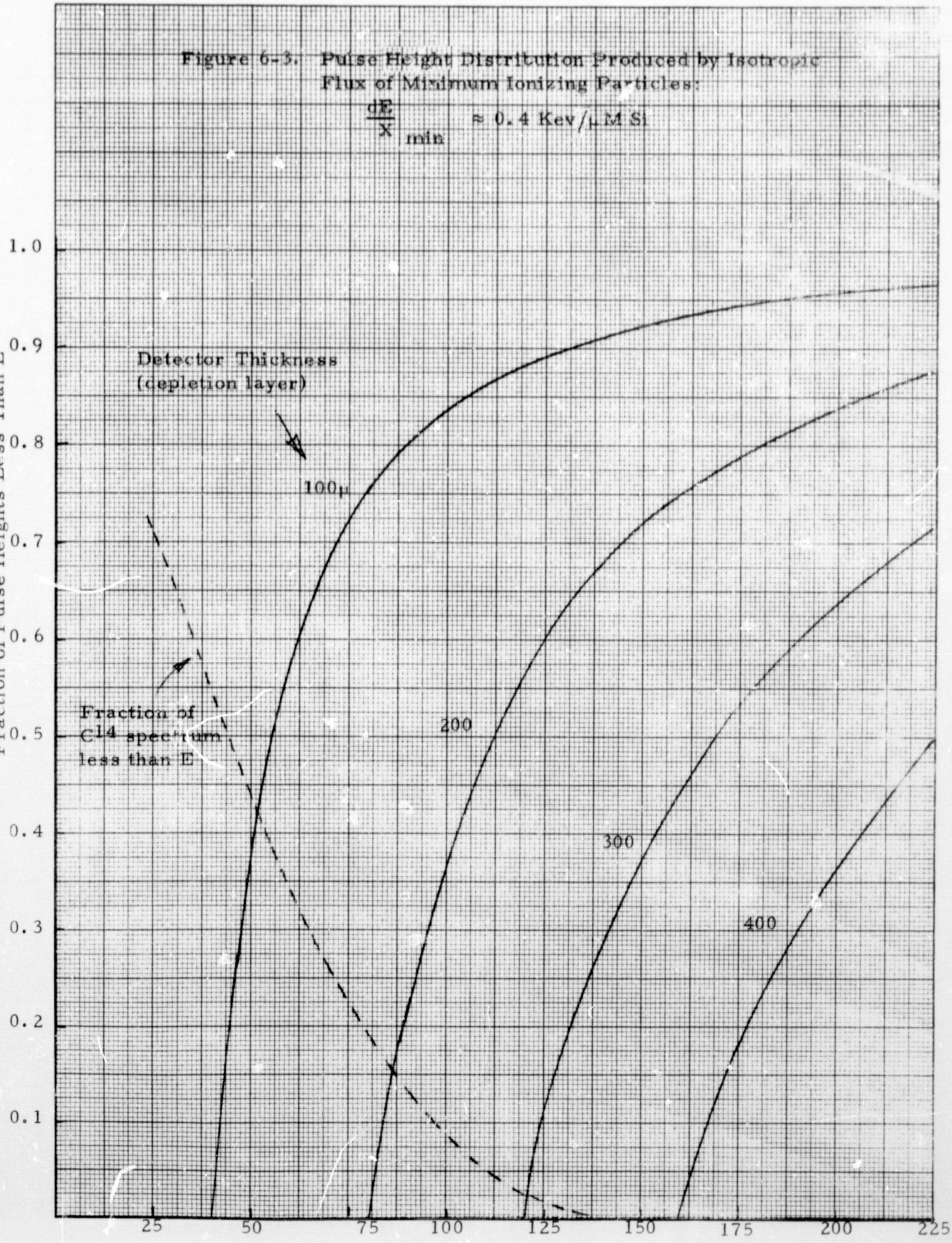

background is considerably smaller than the RTG gamma background. The calculations of cosmic ray background have not included the contribution from solar flare protons because it is assumed that the experiments will be turned off during solar flares. The count rate during a flare can be obtained by multiplying the predicted cosmic ray count rates by the ratio $(x + 4)/4$ where x is the solar flare proton flux (p, ^{2} sec).

SECTION 7

RTG BACKGROUND RATES

RTG background rates are calculated for the gamma ray flux only. The neutron flux is not included in the calculations because its contribution to the count rate is small. In silicon, for example, the average neutron scattering cross section is about 2.5 barns and the total neutron flux from the RTG is 270 n/cm^2-sec. The number of neutron scattering events that will take place in a 300μ thick semiconductor detector is therefore $\sim$1 event/cm^2-sec, which is only about 1/40 of the gamma ray induced count rate. Furthermore, many of the counts that could be produced by silicon atom recoils can be rejected by pulse height analysis. At 2.5 Mev where the neutron flux has peak intensity, about 65% of the recoil atoms will have energies outside of a 30 to 150 Kev window. Also, no neutrons with energy less than 225 Kev will be capable of producing recoil energies greater than 30 Kev and any neutrons which undergo charged particle reactions, which have small cross sections will almost certainly produce pulse heights greater than 150 Kev. The neutron background can therefore be neglected in the semiconductor detector and a similar analysis would show that it is also neglible in the pancake detectors.

The procedures employed to calculate the RTG gamma ray background are described below.

7.1 BACKGROUND COUNT RATE DUE TO GAMMA RAYS IN PANCAKE DETECTORS

The background count rate in the proportional counter was obtained by estimating the probability that a gamma ray interaction in the counter wall will produce a secondary electron which leaks into the sensitive volume of the counter. The formula employed to estimate the count rate produced per unit area of detector wall surface is

$$\frac{\text{Count Rate}}{\text{Area}} = B = \sum_{i=1}^{8} \phi_i \cdot (\mu_i R_i) \cdot \beta_i \qquad (1$$

where ϕ_i is the RTG gamma ray flux in the i^{th} energy group (Table 4-1)

μ_i is the average gamma ray cross section for the i^{th} energy group (photoelectric and Compton events are considered separately)

R_i is the average range of electrons produced by gamma ray interactions in the i^{th} energy group. For Compton events, the estimate of range was based on the maximum Compton electron energy.

β_i is an escape factor which accounts for the probability that electrons produced within a distance R_i of the counter wall will leak into the counter volume. β_i was assumed to be 0.4 for Compton events and 0.25 to 0.5 for photoelectric events.

As indicated in Equation 1, the total count rate is obtained by summation of the contributions from each gamma ray energy group.

Results of the calculation are summarized in Table 7-1 which gives the background count rate for each gamma ray energy group. The results are also compared with count rate predictions based on the formula*

$$\frac{\text{Count Rate}}{\text{Area}} = B = \sum_{i=1}^{8} \phi_i \left(\frac{\mu_\gamma}{\mu_\beta - \mu_\gamma}\right)\left[\exp(-\mu_\gamma x) - \exp(-\mu_\beta x)\right]_i \quad (2$$

where ϕ_i is the RTG gamma ray flux in the i^{th} energy group

μ_γ is the gamma ray mass absorption coefficient

μ_β is the beta ray mass absorption coefficient

x is the counter wall thickness (10 mils)

The results of the two calculations agree fairly well, particularly in the high and low energy groups. While neither calculational procedure is expected to be highly accurate, Equation (1 is expected to be more reliable and was adopted for the calculations.

*EON Corporation detector catalogue.

7.1.1 Total Count Rate in Detector Pair

The total RTG gamma background in a pair of detectors was obtained by multiplying the total count rate by the area of the detectors and making adjustments for the source normalization and shielding, i.e.,

$$\text{Total Count Rate} = (1.2\pi R^2 + 2\pi R^2 t) \cdot 2 \cdot 3 \cdot A \cdot B$$

$$= 6\pi R^2(1.2 + 2t) \cdot A \quad B \qquad (3$$

where R is the detector radius, t the reduced detector thickness (t = linear thickness/Radius), A the attenuation factor provided by lead shielding around the RTG's and B is the calculated background count rate per unit area obtained above. The detector window will be 80% open so it is assumed that the closed area of the window will also be effective in producing background; hence, the factor of 1.2 in the expression for the detector area. The factor of 2 accounts for the number of detectors while the factor of 3 normalizes the source strength to the projected 2400 thermal watts.

In Equation (3, it is assumed that the RTG flux is incident uniformly on all surfaces of the detector; i.e., that the RTG flux is isotropic. In fact, the RTG's are located some distance from the detectors so the flux will not be isotropic and the detectors will provide some self-shielding. However, the self-shielding is only significant for the low energy gamma rays and these are strongly attenuated by lead shielding around the RTG. Therefore, the assumption of isotropic RTG flux does not appear to be serious, if shielding is employed.

The attenuation factor, A, provided by lead shielding was calculated for each gamma ray energy group using the total attenuation coefficient in lead and assuming no buildup of scattered radiation. The results of this calculation are presented in Figure 7-1, and summarized in Table 7-2. In order to avoid buildup of scattered radiation from the lead shield, the shield should be placed near the RTG's. The scattered radiation will then have a greater probability of being scattered out of the primary photon beam before it reaches the detectors.

Figure 7-1. RTG Gamma Count Rates in Pancake Detector Per Unit Area of Detector Wall vs Pb Shield Thickness

Normalized to 800 watt RTG

Equation 2

Equation 1

Total Counts

Counts in each Energy Group (Equation 1)

RTG γ Counts/cm^2 - min

g/cm^2 Pb

1000
100
10
1.0
10^{-1}

1 2 3 4 5 6

1 2 3 4 5 6 7 8

TABLE 7-1

RTG GAMMA BACKGROUND RATES FOR PANCAKE COUNTERS
(NORMALIZED TO 800 THERMAL WATTS)

Gamma Ray Energy Group	Background Rates	
	Based on Equation 1	Based on Equation 2
1	10.9 counts/cm^2-min	9.4 counts/cm^2-min
2	20.4	20.0
3	15.4	20.7
4	13.8	25.6
5	9.9	27.6
6	40.0	101.8
7	23.5	41.1
8	41.5	37.4
Total	175 counts/cm^2-min	285 counts/cm^2-min

TABLE 7-2

EFFECTIVENESS OF LEAD SHIELDING IN REDUCING THE RTG BACKGROUND IN PANCAKE COUNTERS

Thickness of Lead Shield	RTG Background Counting Rate *
0.0 g/cm^2	175 counts/cm^2-min
0.5	80
1.0	62
1.5	54
2.0	50
3.0	44
5.0	36

*Based on Equation 1

7.1.2 Pulse Height Rejection

Pulse height rejection will not be very effective with the small pancake detectors so it has not been included in the estimates of background rates. To be effective, the background radiations must deposit more energy in the detector than the C^{14} betas. Since the dE/dX of secondary electrons and minimum ionizing protons are comparable to the dE/dX of C^{14} betas, the dimensions of the detector must be long compared to the C^{14} end point range in order for pulse height rejection to be effective.

If the fill gas in the detector is Krypton, for maximum stopping power, at 1/2 atmosphere and 10°C, a 150 Kev beta has a range of 10.7 cm and a 100 Kev beta has a range of 5.3 cm. These ranges are long compared to the dimensions of the pancake detectors being considered for the category A experiments so the pulse height rejection efficiency is expected to be quite low. Because it is low and difficult to estimate, it was assumed to be zero in these calculations.

There would be no advantage in increasing detector volume in order to improve pulse height rejection efficiency because both the RTG and cosmic ray background rates will increase in proportion to the detector surface areas.

7.1.3 Coincidence Rejection

The RTG background rate in the pair of detectors will be reduced because of some coincident detection of the recoil electrons. Because of the complexities involved in this process, no attempt was made to estimate the coincidence rate. It is assumed to be zero. This parameter can be evaluated more accurately and easily in the Task II breadboard experiments.

The coincidence rate is also assumed to be zero for pairs of semiconductor detectors. The effect of this assumption will therefore not be too important in comparing the relative merits of the two types of detectors since it will tend to cancel out.

7.1.4 Assessment of Validity of Calculation

The calculation of absolute gamma ray count rate per unit area of detector was considered to be fairly inaccurate and could be in error by a factor of 2. The neglect of self-shielding in the detector should not be serious if RTG shielding is employed. Similarly, the estimates of shielding effectiveness should be fairly good provided buildup is small (shield near RTG and thin).

The greatest uncertainties in the calculation appear to be:

1) the assumption that the coincidence rate between counter pairs is zero.

2) the neglect of count rate produced by electrons created in the walls of the housing for the sample volume located between the pair of detectors.

An attempt should be made to measure or estimate these effects.

7.2 RTG BACKGROUND RATE IN SEMICONDUCTOR DETECTORS

The basic assumption made in estimating the RTG gamma background is that the count rate is proportional to the thickness of the depletion layer. Thus, the count rate per unit area is

$$\text{Count rate/Area} = B = \sum_{i=1}^{8} \phi_i \cdot (\mu_i t)$$

where

ϕ_i is the RTG gamma ray flux in the i^{th} energy group

μ_i is the gamma ray attenuation coefficient for silicon

t is the thickness of the depletion layer.

The calculations of count rate were performed for two different values of the attenuation coefficient. In one case, the attenuation coefficient is assumed to be defined by the total cross section. In the second case, the cross sections were modified to include only that portion of the cross section which results in the production of a secondary electron with energy in the range of 30 to 150 Kev. That is, the photoelectric absorption cross section was assumed to be zero below 30 Kev and above 150 Kev. The Compton cross section was similarly modified to include only those events which produce a 30 to 150 Kev scattered electron. These modified cross sections are appropriate to the case where pulse height rejection is employed to reject pulses other than those in the 30 to 150 Kev range.

The results of the background calculations are summarized in Table 7-3 for the two different assumptions regarding cross section. The depletion

TABLE 7-3

RTG BACKGROUND RATES IN SOLID STATE DETECTORS (300μ DEPLETION LAYER, 800 THERMAL WATTS)

Gamma Ray Energy Group	Background Count Rate	
	Based on Total Cross Section	Based on 30 to 150 Kev Cross Sections
1	10.6 Counts/cm^2-min	1.15 Counts/cm^2-min.
2	38.0	6.92.
3	51.3	16.2
4	104.	54.4
5	160.	114.
6	732	264
7	342	103
8	995	299.
Total	2,430 counts/cm^2-min	860 Counts/cm^2-min

layer thickness employed in the calculation is 300μ and, according to the assumption made above, the count rate scales linearly with the thickness. The count rate obtained when only the 30 to 150 Kev events are considered is approximately 1/3 of that obtained with the total cross section. The ratio remains essentially constant when lead shielding is employed to reduce the background count rate. Data on the effectiveness of the lead shielding is presented in Table 7-4 and plotted in Figure 7-2. The procedure employed to calculate shielding effectiveness is the same as that employed in the pancake detector calculations. The lead shielding is more effective for the solid state detectors than for the pancake detectors because the solid state detectors are more sensitive to low energy gamma rays which are preferentially shielded by the lead.

Figure 7-2 RTG Gamma Interaction Rates in Silicon vs P_b Shielding.

Based on a 300μ depletion depth and the Total Interaction Probability.

RTG Source Strength 800 Thermal Watts.

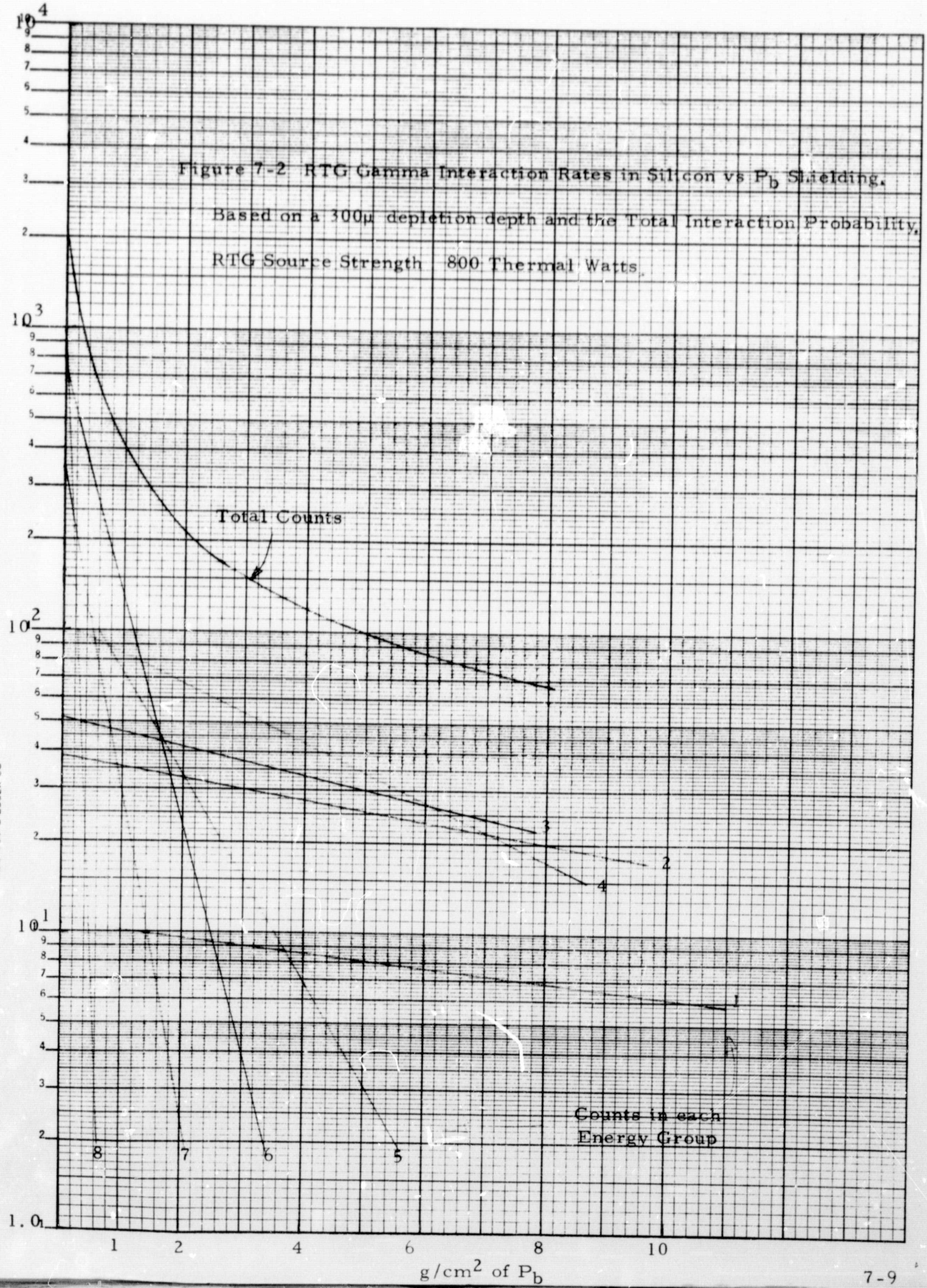

TABLE 7-4

EFFECTIVENESS OF LEAD SHIELDING WITH SOLID STATE DETECTORS

Lead Shield Thickness	Total Cross Section	30-150 Kev Cross Section
0 g/cm^2	2,430 counts/cm^2-min	860 counts/cm^2-min
0.5	720	250
1.0	405	140
2.0	210	79
4.0	120	43

7.2.1 Total Count Rate in Pair of Detectors

The total RTG gamma count rate in a pair of detectors is obtained by multiplying, B, the estimated rate per unit area, by the area of the detectors and correcting for source normalization and depletion layer thickness.

$$\text{Total RTG Count rate} = 2\pi R^2 B \cdot \frac{t}{300} \cdot 3 = 2\pi R^2 B\tau$$

where τ is the detector thickness in 100's of microns.

7.2.2 Pulse Height Rejection

Pulse height rejection efficiency in semiconductor detectors was estimated by employing only that portion of the gamma ray interaction cross sections which result in the production of secondary electrons with energy in the range of 30 to 150 Kev. The results obtained with this procedure have been presented in the previous section.

This procedure for estimating pulse height rejection efficiency provides a first order estimate of rejection efficiency but is not expected to be accurate since it does not account for electron transport into or out of the depletion layer. The effects of electron transport may tend to cancel in that

the number of electrons which fall into the 30 to 150 Kev window as a result of transport will be diminished by electrons that deposit less than 30 Kev before leaving the depletion layer. In any event, a more rigorous evaluation of rejection efficiency is not within the scope of the contract and rejection efficiency can be measured more accurately and easily in the Task II breadboard evaluation.

Pulse height rejection is not expected to be efficient in thin detectors because the electrons are unlikely to deposit 150 Kev or more of energy before they escape from the depletion layer. The range of a 150 Kev electron in silicon is 100 μ so pulse height rejection should be effective for depletion layer thickness greater than 100μ.

7.2.3 Coincidence Rejection

No attempt was made to estimate coincidence rejection efficiency for a pair of semiconductor detectors. Coincidence rejection was also neglected for pairs of pancake detectors so the effect of the omission of this factor should tend to cancel when comparisons are made between the various types of detectors.

7.2.4 Validity of the Calculation

The validity of the RTG background calculations for the solid state detectors is subject to the same uncertainties involved in the pancake detector. The most critical assumptions being

1) the assumption that the coincidence rate between detector pairs is zero,

2) the neglect of background produced by electrons created in the walls of the housing for the gas sample.

These assumptions should have about the same effect on both types of detectors. The effect of these uncertainties is therefore not too important in comparing the relative merits of the two types of detectors since they tend to cancel out.

However, assumption that the count rate in a solid state detector is proportional to the interaction rate in the depletion volume can be

seriously questioned. There will undoubtedly be counts produced by events that occur outside of the depletion layer but produce an electron which travels into the depletion layer to produce a count. It is difficult to estimate the importance of these types of events because pulse height rejection can effectively be employed to reject small pulses ($\lesssim$ 30 Kev produced by electrons which just barely get into the depletion layer) and very large pulses ($\gtrsim$150 Kev produced by electrons which travel more than 100μ in the depletion layer).

Experiments conducted with a surface barrier detector using Cs^{137} (666 Kev) and Mn^{54} (835 Kev) indicate that the total count rate in the detector is indeed proportional to the thickness of the depletion layer; at least, in the range from 100μ to 300μ. However, the observed count rate is considerably higher than would be predicted on the basis of the depletion layer thickness. It is not clear at this time whether the descrepancy is due to gamma ray scattering from the walls of the detector housing (thus increasing the effective geometric efficiency for the experimental setup) or due to events that occur inside the detector but outside the depletion layer, as described above. Further attempts will be made to resolve the source of discrepancy.

SECTION 8

THE FIGURE OF MERIT, $R_s/\sqrt{R_B}$

The evaluation of detector performance is based on the parameter $R_s/\sqrt{R_B}$ where R_s is the signal count rate and R_B is the background count rate in the detector. When this figure of merit is maximized, the detector design is optimized. The discussion presented in the following paragraphs demonstrates that the figure of merit is a good measure of detector performance and is more valid than other measures such as the signal-to-noise ratio. The relationship of the figure of merit to the detectability of the signal is also discussed.

8.1 DERIVATION OF FIGURE OF MERIT

The figure of merit can be derived by considering a counting experiment in which a background count rate R_B is monitored for a counting period t_B, and a combined background plus signal count rate, $R_A = R_B + R_s$, is monitored for a time period t_A. If the total counting time $T = t_A + t_B$ is fixed, the problem is to determine the optimum partition of the counting times t_A and t_B such that the variance to mean ratio of the estimate of the signal count rate R_s will be minimum; i.e., the signal is to be measured with the greatest possible accuracy in the allotted time.

If the background is monitored for a time t_B, the total background count will be $B = R_B \cdot t_B$ and the expected variance in this count is equal to $\sqrt{B}$. The corresponding variance ρ_B in the background count rate R_B is therefore:

$$\rho_B = \frac{\sqrt{B}}{t_B} = \sqrt{R_B/t_B} \qquad (1)$$

and an analogous expression applies to variance ρ_A to be expected in the measurement of the combined background and signal count rate.

Having measured R_A and R_B, the estimate of the signal count rate R_s is

$$R_s = R_A - R_B \qquad (2)$$

and the variance of the estimate, ρ_s, is

$$\rho_s = \sqrt{\rho_A^2 + \rho_B^2} \tag{3}$$

Substituting from Equation 1, the expression for ρ_s can be written

$$\rho_s = \sqrt{\frac{R_A}{t_A} + \frac{R_B}{T - t_A}} \tag{4}$$

The condition for minimizing ρ_s is obtained by setting its derivative with respect to t_A equal to zero, which results in the equation

$$\frac{t_A}{t_B} = \left(\frac{R_A}{R_B}\right)^{1/2} \tag{5}$$

The variance is therefore minimized by partioning the counting times in proportion to the square roots of the respective counting rates.

From Equation 5, it follows that

$$T = t_A + t_B = t_A \left[1 + \sqrt{\frac{R_B}{R_A}}\right] \tag{6}$$

or

$$t_A = T \left[1 + \sqrt{R_B/R_A}\right]^{-1}$$

and similarly

$$t_B = T \left[1 + \sqrt{R_A/R_B}\right]^{-1} \tag{7}$$

Substituting Equation 6 and 7 into Equation 4 gives the expression for the minimum possible variance in the estimate of the signal count rate obtainable in time T

$$\rho_s^{\min} = \frac{\sqrt{R_A} + \sqrt{R_B}}{\sqrt{T}} = \frac{\sqrt{R_B + R_s} + \sqrt{R_B}}{\sqrt{T}} \qquad (8)$$

The minimum possible percentage error in the estimate of the signal count rate is therefore

$$\left(\frac{\rho_s}{R_s}\right)_{\min} = \frac{\sqrt{R_A + R_s} + \sqrt{R_B}}{R_s\sqrt{T}} = \frac{\sqrt{R_B}}{R_s\sqrt{T}}\left(1 + \sqrt{1 + R_s/R_B}\right) \qquad (9)$$

When the signal-to-noise ratio is small (the condition that will most likely occur in the life detection experiments on Mars) the variance to mean ratio of the signal count rate becomes

$$\left(\frac{\rho_s}{R_s}\right)_{\min} \approx \frac{2}{\sqrt{T}} \frac{\sqrt{R_B}}{R_s} \qquad (10)$$

Thus, Equation 10 shows that, to make the most accurate determination of the signal count rate, the figure of merit $R_s/\sqrt{R_B}$ should be maximized. In terms of detection accuracy, the figure of merit is therefore a valid measure of detector performance.

From Equation 9, it follows that the figure of merit is no longer a good, single-measure of detector performance when the signal-to-noise ratio is much larger than unity. However, if the signal-to-noise is very large, it will be easy to detect the signal and optimization of detector design is not of crucial importance

8.2 DETECTION ACCURACY WITH EQUAL COUNTING PERIODS

The discussion above was based on the optimum partition of counting time during the experiment. It is doubtful that the counting periods will be optimized when the life detection experiments are conducted on the Martian surface. More likely, the two counting periods will be of equal duration so it is useful to consider the effect of equal counting periods on the detector performance.

In a counting time T/2, the total counts recorded in each counting period will be $A = R_A \cdot T/2$ and $B = R_B \cdot T/2$. The expected variance in these two counts is $\sqrt{A}$ and $\sqrt{B}$. The variance to mean ratio for the signal count, or count rate, is therefore

$$\frac{\rho_s}{R_s} = \frac{\sqrt{A+B}}{A-B} = \frac{2\sqrt{R_B}}{R_s\sqrt{T}}\sqrt{1+\frac{R_s}{2R_B}} \qquad (11)$$

This percentage error in the measurement of R_s therefore has the same dependence on the figure of merit and total counting time as obtained with the optimized partition of counting periods in Equation 9. However, the multiplicative factor, which depends on the signal-to-noise ratio, is different. The importance of the multiplicative factor can be evaluated by computing the ratio of the two expressions.

$$\text{Ratio} = \frac{\left(\frac{\rho_s}{R_s}\right)_{\text{equal t}}}{\left(\frac{\rho_s}{R_s}\right)_{\text{opt t}}} = \frac{2\sqrt{1+0.5\,R_s/R_B}}{1+\sqrt{1+R_s/R_B}} \qquad (12)$$

For very small signal to noise ratio, the square roots can be approximated by the first order terms in the series expansion, so that

$$\text{Ratio} \xrightarrow[\frac{R_s}{R_B} \ll 1]{} \frac{2\left(1+\frac{R_s}{4R_B}\right)}{1+1+\frac{R_s}{2R_B}} = 1 \qquad (13)$$

Thus, for small signal-to-noise ratios, equal counting periods will produce essentially the same detection accuracy as the optimum procedure. This is to be expected since it follows from equation 5 that, in the limit as the signal-to-noise ratio goes to zero, equal counting periods are also the optimum counting periods.

The Ratio in Equation 12 has also been evaluated for several values of signal-to-noise and the results are presented in Table 8-1.

TABLE 8-1

RATIO OF COUNTING ACCURACIES OBTAINED WITH EQUAL AND OPTIMIZED COUNTING PERIODS

Signal to Noise, R_s/R_B	Ratio of Accuracies (Eq. 12)
0	1.
0.1	1.0003
0.5	1.005
1.0	1.015
2.0	1.035
10.0	1.135

The values of the ratio show that the difference between the optimum counting periods and equal counting periods is not important for the small signal-to-noise levels likely to be encountered in the Martian experiments. For example, at a signal to noise ratio of 1, the accuracy obtained with the optimum counting time is only 1.5% better than that obtained with equal times. Even at a signal-to-noise ratio of 10, the accuracy is only 13.5% better. Therefore, for purposes of detection accuracy, equal counting periods are essentially equivalent to optimally partitioned counting periods and it is not essential to distinguish between the two types of counting procedures. The terms can, with only small inaccuracy, be used interchangably.

8.3 FIGURE OF MERIT AS A MEASURE OF DETECTOR SENSITIVITY

It has been shown that the figure of merit provides a measure of the accuracy with which a signal count rate can be detected. However, the derivation of the figure of merit provides no indication of the reliability or confidence that can be placed on the result of a particular experiment. For example, if a signal is present, the difference between count A (signal plus background) and count B (background only) can be attributed to the signal and the accuracy in this estimate of the signal count is $\sqrt{A + B}$. However, because of random fluctuations in the background, it may also be possible to observe the same counts, A and B, even though no signal is present during the accumulation of count A. In this event, one would deduce the same signal intensity (A-B) and variance $\sqrt{A + B}$ as before; but it would be erroneous to attribute the difference in counts to the presence of a real signal. Therefore, one cannot place 100% confidence in the results of a counting experiment but, as will be shown below, the numerical value of the figure of merit does provide a measure of the confidence that can be placed on a particular experimental result.

If the mean background count expected in the counting period is B, the probability of observing a count y is (assuming a gaussian distribution)

$$P_B(y) \cdot dy = (2\pi B)^{-1/2} \exp\left[-\frac{(y-B)^2}{2B}\right] dy \qquad (14)$$

Similarly, the probability of observing a signal plus background count, x is

$$P_A(x) \cdot dx = (2\pi A)^{-1/2} \exp\left[-\frac{(x-A)^2}{2A}\right] \cdot dx \qquad (15)$$

where A is the mean number of counts expected and $A = B + S$ where S is the mean number of signal counts. The difference in the two observed counts, s, is

$$s = x - y \qquad (16)$$

and it is desired to calculate the probability $\Phi_1(s)$ that the value of s will lie in ds about s. The probability can be calculated by evaluating the integral

$$\phi_1(s) = N \cdot \int_{-\infty}^{\infty} P_B(y) \cdot P_A(x = y + s)\, dy \qquad (17)$$

where N is a normalization constant. The result can also be obtained by noting that the difference of two variates from two different gaussian distributions is itself a gaussian distribution with variance equal to the sum of the variances of the two gaussian distributions; i.e.,

$$\phi_1(s) \cdot ds = (2\pi(A + B))^{-1/2} \exp\left[-\frac{(s - S)^2}{2(A+B)}\right] ds$$

$$= (2\pi(2B + S))^{-1/2} \exp\left[-\frac{(s - S)^2}{2(2B + S)}\right] ds \qquad (18)$$

Similarly, the probability of observing a difference r between two background measurements (i.e., no signal is present during signal plus background measurement so A = B) is

$$\phi_2(r) \cdot dr = (4\pi B)^{1/2} \exp\left(-\frac{r^2}{4B}\right) \cdot dr \qquad (19)$$

Thus, when the life detection experiment is performed, the difference in the two observed counts will be distributed according to Equation 19 if there is no C^{14} signal and according to Equation 18 if there are S signal counts, on the average, during the counting period.*

To compare the two distributions, it is convenient to define the parameter

$$Z = \frac{r}{2\sqrt{B}} \quad \text{or} \quad Z = \frac{s}{2\sqrt{B}} \qquad (20)$$

*It is assumed that the two counting periods are of equal duration. The equations could be generalized to account for unequal counting periods but the added complication is not warranted in view of the discussion in Section 8.2.

The distribution function for the count difference obtained with no signal present is then

$$\phi_2(Z) = \pi^{-1/2} \exp(-Z^2) \tag{21}$$

and the distribution function $\phi_1(s)$ for differences obtained with signal counts present is

$$\phi_1(Z) = \left(\frac{1}{\pi} \quad \frac{1}{1 + S/2B}\right)^{1/2} \exp\left[\frac{-(Z - \frac{S}{2\sqrt{B}})^2}{1 + S/2B}\right] \tag{22}$$

One can then define a modified figure of merit, M,

$$M = S/\sqrt{B} = \frac{R_s \sqrt{T}}{\sqrt{R_B}} \tag{23}$$

where this modified figure of merit is equal to the original figure of merit defined above, $R_s/\sqrt{R_B}$, multiplied by the square root of the total counting time. Note that the time factor enters the definition of the modified figure of merit in the same relative position that it appears in the expression for detection accuracy in Equations 9 and 11. Employing this definition of M, and assuming that the signal-to-noise ratio, S/B, is small, the distribution function $\phi_1(z)$ becomes

$$\phi_1(z) \cong \pi^{-1/2} \exp\left[-(Z - \frac{M}{2})^2\right] \tag{24}$$

The distribution $\phi_1(z)$ is therefore identical to $\phi_2(z)$ except that the centroid of the distribution is displaced a distance M/2 from the origin. Figure 8-1 for example shows a plot of $\phi_1(z)$ for M = 2 with a plot of $\phi_2(z)$ also included for comparison. The two distributions have overlapping areas and illustrate the problem that can arise in data interpretation when the figure of merit is small. For example, it follows from the figure that if the life detection measurements result in a value of Z = 0.5, the result could, with equal probability, be due to random fluctuations in background or it could be due to the presence of a C^{14} signal of such magnitude that M = 2.

Figure 8-1 Distribution $\phi_1(z)$ and $\phi_2(z)$ for Count Differences

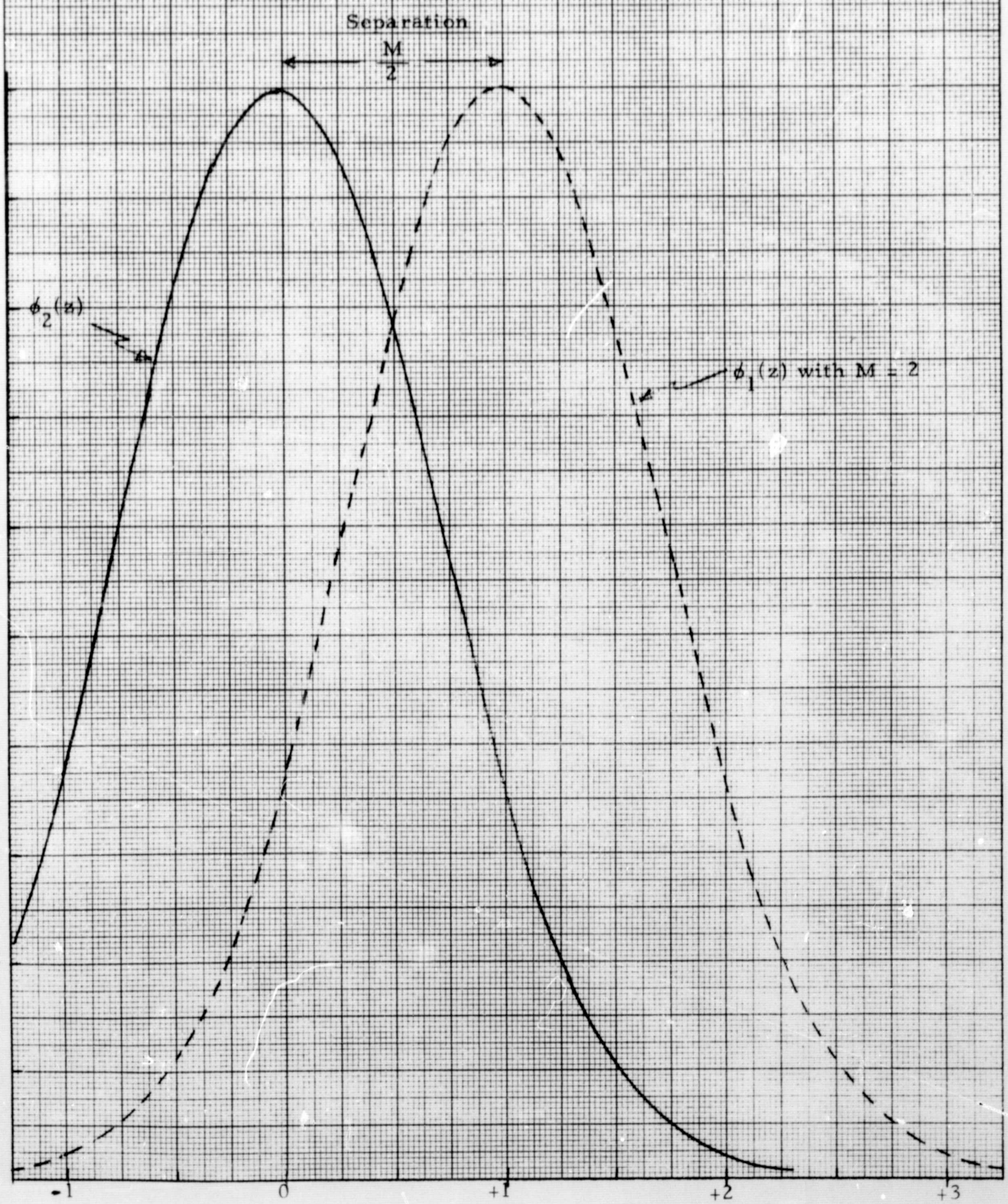

Since the separation between the centroids of the $\phi_1(z)$ and $\phi_2(z)$ distribution is equal to M/2, the results of the experiments will be ambiguous unless M is sufficiently large to preclude, or at least minimize, the degree of overlap between the two distributions. In order to utilize this factor in the design of the C^{14} detector systems, the relationship between the figure of merit and degree of overlap must be quantified.

One procedure that can be employed to measure the degree of overlap between the two distribution is to form the product of the two distributions and calculate the area under the product curve; thus

$$\text{Area of Product Curve} = \int \phi_1(z) \cdot \phi_2(z) \cdot dz \qquad (25)$$

$$= \left(\frac{1}{8\pi B}\right)^{1/2} \left(\frac{1}{1 + \frac{M}{4\sqrt{B}}}\right)^{1/2} \exp\left[-\frac{M^2}{8}\left(\frac{1}{1 + \frac{M}{4\sqrt{B}}}\right)\right]$$

If M = 0 (i.e., one considers the product $\phi_2(z)^2$ rather than $\phi_1(z) \cdot \phi_2(z)$), the area under the curve is $(8\pi B)^{-1/2}$. Thus, the result obtained in Equation 25 should be normalized by multiplying it by $(8\pi B)^{-1/2}$ and the result will then be a quasi-probability function for the degree of overlap, i.e.,

$$\text{Degree of Overlap} = \left(\frac{1}{1 + \frac{M}{4\sqrt{B}}}\right)^{1/2} \exp\left[-\frac{M^2}{8}\left(\frac{1}{1 + \frac{M}{4\sqrt{B}}}\right)\right] \qquad (26)$$

This "Degree of overlap" is plotted as a function of M for $\sqrt{B}$ very large ($>> 10$) and for $\sqrt{B} = 10$. In Figure 8-2 the curves show that if the "degree of overlap" is to be 10^{-3} or less, then M must be larger than 7.5

A statistically more valid procedure for measuring the degree of overlap between the two distributions is to first select a value of z; say z = X. This value of X will be used as the criteria for determining whether or not a valid C^{14} signal is present during the counting experiment. If the measured value of Z is greater than X, it would be concluded that C^{14} signal is present and a value of Z less than X would indicate that no C^{14}

Figure 8-2 Degree of Overlap vs
Modified Figure of Merit

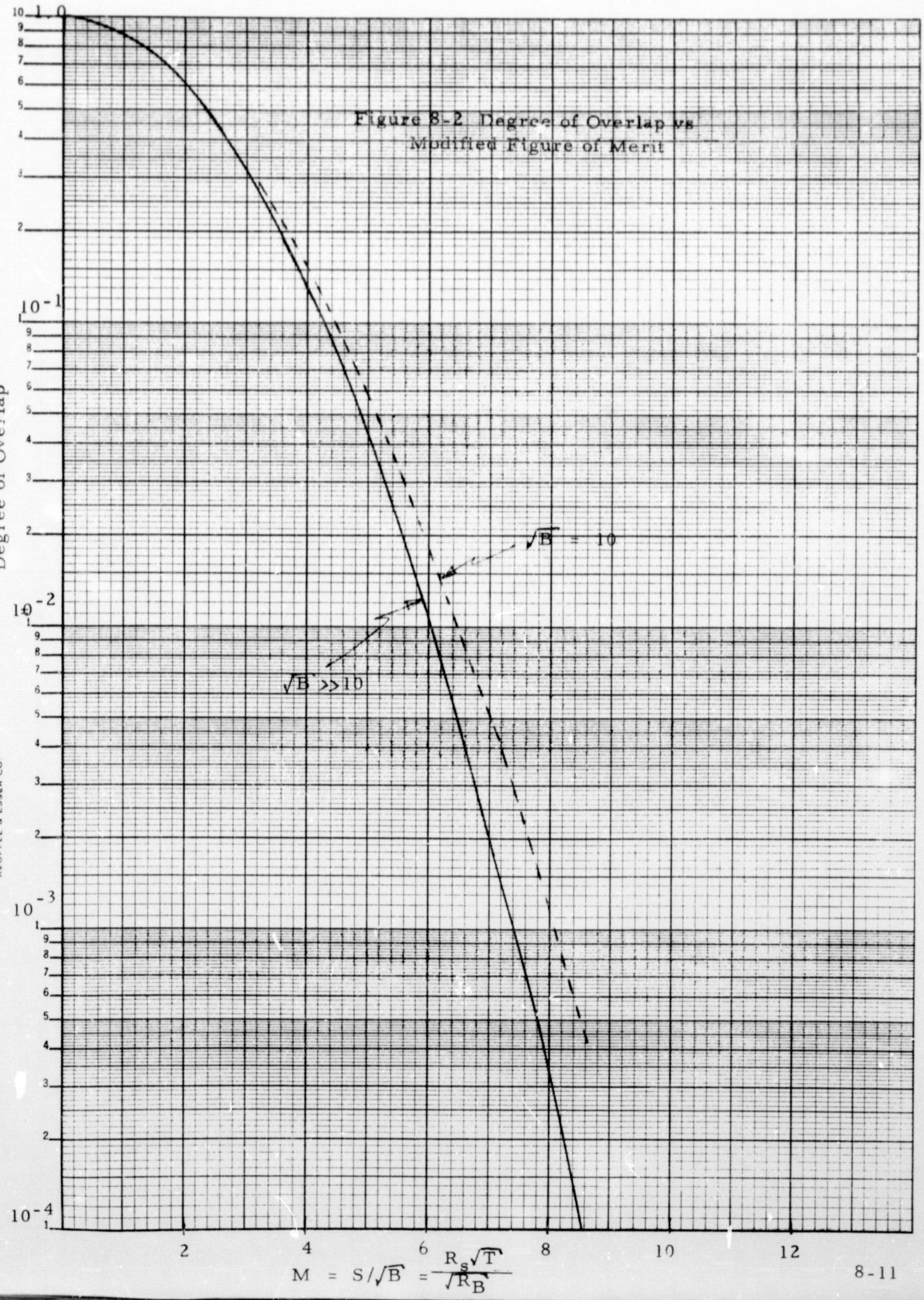

is present. If this procedure is adopted, it is important to know the probability, $P_1(Z \leq X)$, that a valid C^{14} signal will be so small that it will not be properly identified and the corresponding probability, $P_2(Z \geq X)$, that an unusually large background signal will erroneously identified as valid signal. These probabilities can be evaluated from the distribution functions $\phi_1(Z)$ and $\phi_2(Z)$ and their interrelationship is displayed in Figure 8-3 where $P_1(Z \leq X)$ is plotted as a function of $P_2(Z \geq X)$ for several different values of M. The solid lines in the figure assume $\sqrt{B} \geq 10$ whereas the two dashed lines are based on $\sqrt{B} = 10$. The data in the figure show, for example that if the value X is chosen so that $P_2(Z \geq X) = 10^{-3}$, then $P_1(Z \leq X) = 1.8 \times 10^{-3}$ for $M = 6\sqrt{2}$. In terms of the counting experiment, this would mean that, if X is chosen so that the probability of erroneously identifying a background count as a C^{14} signal is 10^{-3}, then the probability that an actual C^{14} signal of such strength that $M = 6\sqrt{2}$ or $S = 6\sqrt{2B}$ will not be properly identified is 1.8×10^{-3}.

In summary, the analysis of the distribution functions for count differences has shown that the modified figure of merit M,

$$M = \frac{S}{\sqrt{B}} = \frac{R_S\sqrt{T}}{\sqrt{R_B}},$$

determines the degree of separation between the ϕ_1 and ϕ_2 distributions*. If M is small, the separation between the distributions is also small and interpretation of the count differences observed in the life detection experiment will be ambiguous (the observed count difference may be due to the presence of C^{14} signal or it may only be due to a fluctuation in background measurements). If M is large ($\gtrsim 8$), the separation between the distributions is also large and the interpretation of the count difference will be much less ambiguous. Thus, the figure of merit, $R_s/\sqrt{R_B}$, not only provides a measure of the counting accuracy but also provides a measure of the probability that the C^{14} signal will be correctly identified. The quantitative relationship between the figure of merit and detectability of the signal are considered in the next section.

*ϕ_1 is the distribution of count differences obtained with signal count present and ϕ_2 is the distribution of count differences obtained when only background is present.

Figure 8-3 $P_1(z \leq X)$ vs $P_2(z \geq X)$

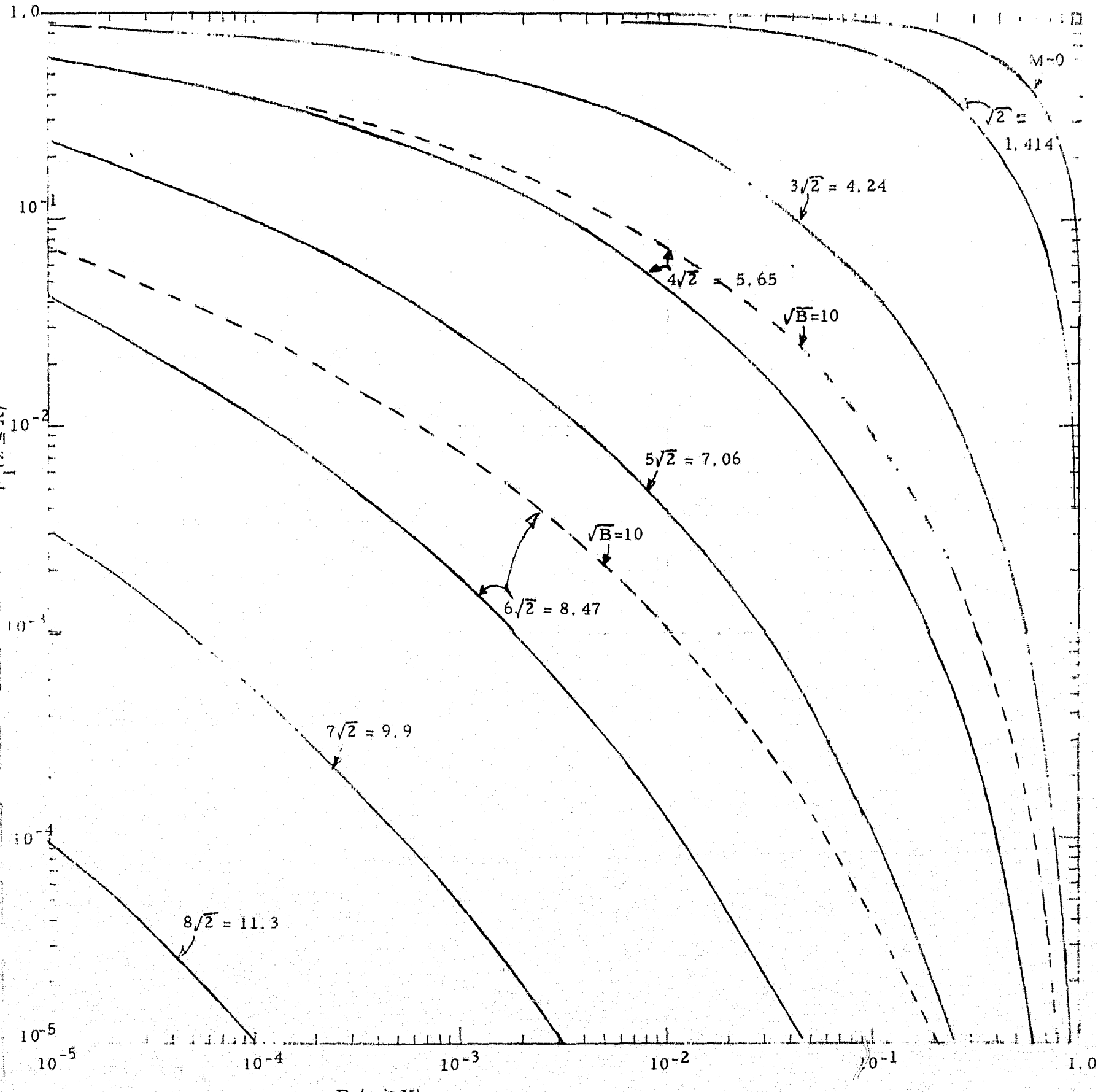

8.4 DETECTION PROBABILITY AND DETECTION ACCURACY

It has been shown that the modified figure of merit determines the separation between the ϕ_1 and ϕ_2 distribution for count differences. It therefore also determines the detection probability; i.e., the probability that a valid C^{14} signal will be correctly identified, and the false detection probability, i.e., the probability that a background signal will erroneously be identified as a C^{14} signal. The definition of the modified figure of merit in Equation 23 can therefore be employed to determine the minimum C^{14} signal that can be detected under specified conditions of background count rate, counting time, and detection probabilities; namely

$$\text{Minimum Detectable } R_s = M\sqrt{\frac{R_B}{T}} \tag{27}$$

The value of M is dependent on the count difference criteria, X, introduced in Section 1.3, and defined by the equation

$$P_2(Z \geq X) = \int_X^\infty \phi_2(Z) \cdot dZ \tag{28}$$

where $P_2(Z \geq X)$ is the desired value for the false detection probability. From the definition of Z in Equation 20, it follows that

$$X = \frac{r_o}{2\sqrt{B}} \tag{29}$$

or, X is the count difference measured in units of the standard deviation of the ϕ_2 distribution. To obtain a convenient expression for M, it will be assumed that

$$P_1(Z \leq X) = P_2(Z \geq X) \tag{30}$$

That is, the probability of failing to detect a valid C^{14} signal will be made equal to the probability of a false detection. In this case, the value of the modified figure of merit becomes

$$M = 2\sqrt{2}X \tag{31}$$

The relationship between the false and failure detection probabilities, $P_2(Z \geq X)$ and $P_1(Z \leq X)$, and the modified figure of merit is illustrated in Figure 8-4. A secondary scale on the abscissa also illustrates the dependence of $P_2(Z \geq X)$ on X. A third scale shows dependence of these probabilities on the figure of merit $R_s/\sqrt{R_B}$ for counting periods of T = 1 hour. The scale indicates that when $R_s/\sqrt{R_B} = 1.0$, the detection probabilities are 3×10^{-3}. This condition provides a convenient relationship for determining the minimum detectable C^{14} count rate, namely

$$\text{Minimum Detectable } R_s = \sqrt{R_B} \tag{32}$$

This condition for minimum detectable signal count rate has been employed in the evaluation of detector performance. As indicated above, it is based on 1 hour counting periods and will result in 3×10^{-3} probability for failing to detect the specified C^{14} signal strength and an equal probability of obtaining a false signal indication when none is present. Other conditions for the minimum detectable R_s could also be obtained by changing the detection probability. For example, $R_s = 0.6\sqrt{R_B}$ for detection probabilities of 5×10^{-2}.

The accuracy with which the signal count rate can be detected was given in Equation 9. Expressed in terms of the modified figure of merit, the detection accuracy is

$$\left(\frac{\rho_s}{R_s}\right)_{min} = \frac{1}{M}\left[1 + \sqrt{1 + M/\sqrt{B}}\right] \tag{33}$$

When $\sqrt{B} \gg M$, where B is the total background count, it follows that

$$\left(\frac{\rho_s}{R_s}\right)_{min} \approx \frac{2}{M}$$

This equation for detection accuracy is also plotted in Figure 8-4. The curve shows that the detection criterion expressed in Equation 32 will result in a detection accuracy of approximately $\pm$ 25%. The curve also indicates that detection accuracies of $\pm$ 20% or less will result in essentially zero values for the false and failure detection probabilities. Therefore, it is not really necessary to achieve detection accuracies better than $\pm$ 20% unless the increased accuracy is required in the biological evaluation of the results.

Figure 8-4 Detection Probability and Detection Accuracy vs Figure of Merit

$P_2(z \geq X)$, $P_1(z \leq X)$

Detection Accuracy (percent ρ_s/R_s)

Detection Accuracy

Detection Probability

Detection probability refers to either the probability of failing to detect a valid C^{14} signal or the probability of making a false detection

$X = \frac{\text{Count Difference}}{2(\text{background})^{1/2}}$

$M = R_s/\sqrt{R_B}$ for T = 60 min

$M = R_s\sqrt{T/R_B}$

APPENDIX A

GEOMETRY CALCULATION FOR A RECTANGULAR ARRAY

The avalanche detectors being investigated under the Life Detection contract were made rectangular in order to use the most uniformly doped region of the silicon wafer and to facilitate construction of a detector array. In order to compare calculated results with experimental measurements, the solid angle efficiency and the cosmic ray shielding efficiency for a rectangular array of six detectors was calculated. The array is depicted in Figure A-1.

A.1 COINCIDENCE RATE

Following the method of Section 6, the total cosmic ray count rate for the detector array will be:

$$\text{Count Rate} = S/4 \cdot (\text{Surface Area})$$

For the array of six avalanche detectors this becomes

$$\text{Count Rate} = 3\,S(\quad \cdot w)$$

where S is the isotropic proton flux assumed to be 4 protons/cm^2-sec. The length and width of the avalanche detector, and w, is 1.6 and 0.635cm respectively. The coincidence rate is given by

$$\text{Coincidence Rate} = S/4 \cdot A \cdot F \cdot 2$$

where

A = surface area of detector No. 1 that can be viewed by Detector No. 2.

F = is the view factor and the additional factor of two accounts for the fact that coincidences may be caused by protons either entering or leaving Detector No. 1.

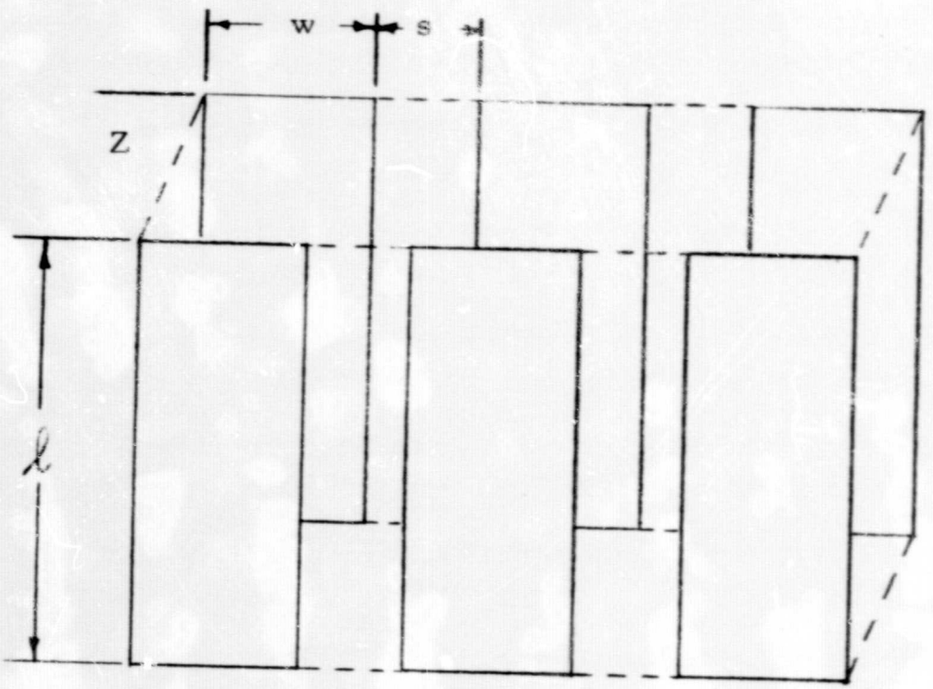

ℓ = 0.63"
w = 0.25"
s = 0.22"

Figure A-1 Rectangular Detector Array

The view factors were calculated for the array shown in Figure A-1, and the results are shown in Figure A-2. The calculations were performed on the Bendix IBM 360 using an existing heat transfer program. The cosmic ray count rate after coincidence is given in Table A-1.

TABLE A-1

COSMIC RAY COUNT RATES IN RECTANGULAR ARRAY*

Array Separation (inches)	Count Rate (Counts per Minute)	
	Before Coincidence	After Coincidence
0.125	720	328
0.250	720	468
0.375	720	538
0.500	720	580

*Six detectors 0.25" wide x 0.63" long. Separation between center and end detector is 0.22".

A.2 GEOMETRIC EFFICIENCY

A Fortran IV program was written to calculate the average solid angle subtended in the sensitive volume by the array shown in Figure A-1. The solid angle subtended by a rectangle of length a and width b from a point located a distance c perpendicularly above one corner of the rectangle is given by[1]

$$\Omega(c) = \mathrm{Tan}^{-1} \frac{a\,b}{c\sqrt{a^2 + b^2 + c^2}} .$$

Using this expression the solid angle subtended by the sensitive areas of the array was calculated for points within the sensitive volume and the average taken. The resulting geometric efficiencies are tabulated in Table A-2.

Taking the average measured value for the intrinsic efficiency of the avalanche detector to be 30% and considering a 1 cm^3 dead volume, the calculated net efficiency for this detector array is, for Z = .25", 7.4%.

[1] Crawford RSI 24 (1953)

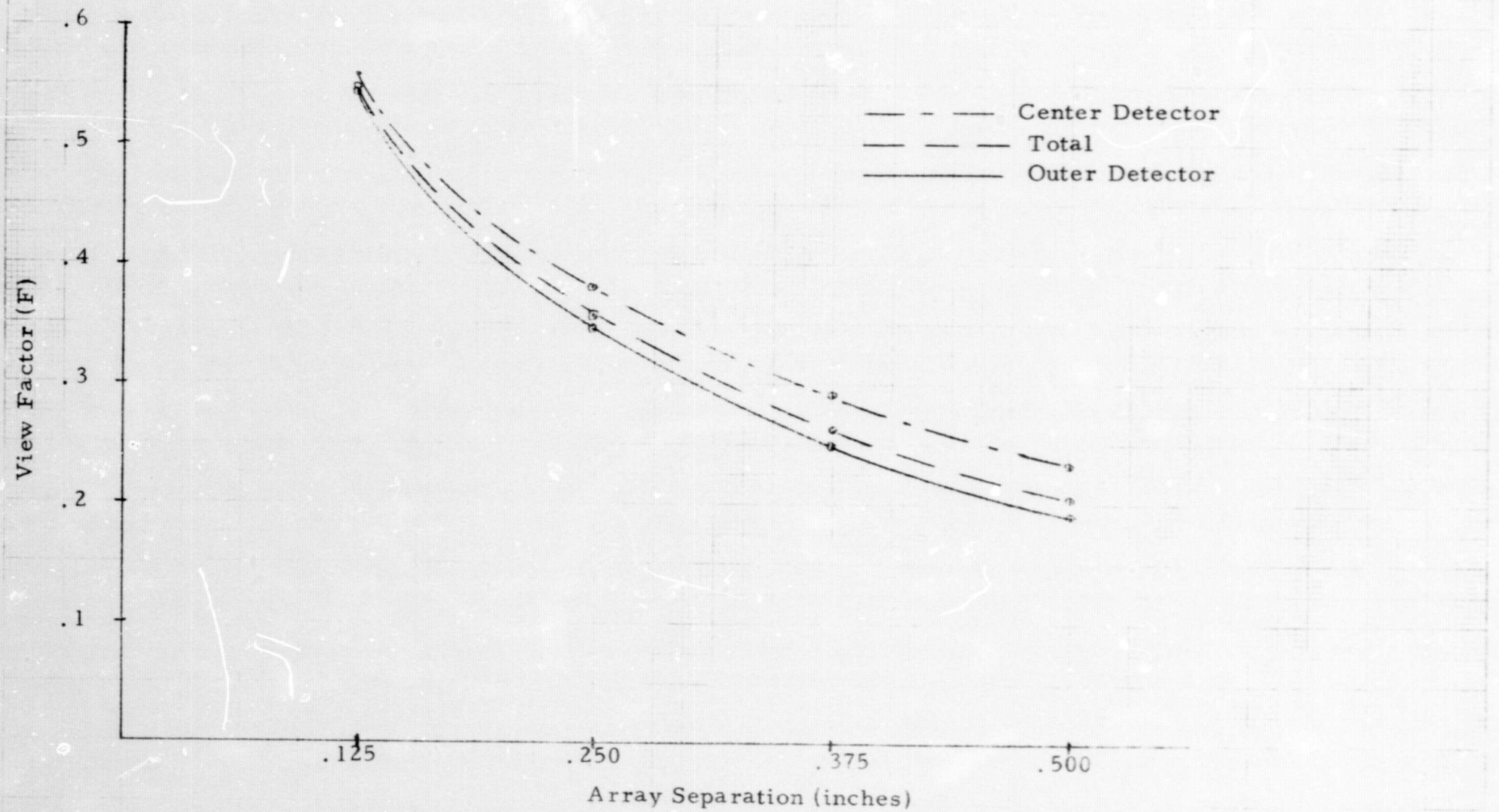

Figure A-2 View Factor for Rectangular Array

TABLE A-2

GEOMETRIC EFFICIENCY, ϵ_g, FOR A RECTANGULAR ARRAY

Array Separation (inches)	ϵ_g*
0.0	1.0
.05	0.47
.1	0.42
.2	0.36
.3	0.31
.4	0.28
.5	0.26
.6	0.23
.7	0.21

*ϵ_g is the fraction of the isotropic radiation occuring within the sensitive volume which is intercepted by one of the six detectors in the array. See Figure A-1. Absorption by the gas is neglected.